周虹利，李鑫，邓阳凡，朱晟. 2025. 联合天然源电磁探测与岩石物理实验约束深地挥发份分布的研究综述[J]. 地球与行星物理论评（中英文），56(6)：641-664. doi：10.19975/j.dqyxx.2025-005.
Zhou H L, Li X, Deng Y F, Zhu S. 2025. A review of studies combining natural-source electromagnetic soundings and petrophysical experiments to constrain the volatile distribution in the deep earth[J]. Reviews of Geophysics and Planetary Physics, 56(6): 641-664 (in Chinese). doi:10.19975/j.dqyxx.2025-005.

联合天然源电磁探测与岩石物理实验约束深地挥发份分布的研究综述

周虹利[1,2]，李　鑫[1*]，邓阳凡[1*]，朱　晟[1,2]
1 中国科学院广州地球化学研究所 深地过程与战略矿产资源全国重点实验室，广州 510640
2 中国科学院大学 地球与行星科学学院，北京 100049

摘要：挥发份（H_2O、CO_2 等）是控制地球内部多圈层系统物理-化学性质及动力学过程的关键因素，在板块构造、岩浆-成矿活动乃至地球宜居环境演化中发挥重要作用. 由于挥发份会显著改变壳幔岩石的物理属性，结合地球物理深部探测与高温高压岩石物理实验是目前获取地球内部挥发份含量分布的主要手段. 在诸多物理属性中，电导率对微量挥发份物质的存在及含量变化尤为敏感，因此利用大地电磁测深（MT）、地磁测深（GDS）等天然场源电磁探测获取的深部电导率结构可为约束壳幔挥发份含量分布提供关键观测约束. 本文首先概述了主要天然场源电磁测深方法的基本原理及特性，并详细介绍了壳幔常见矿物/岩石及熔体的高温高压电导率实验结果，进而回顾了在不同地质构造背景下结合二者开展深部挥发份分布研究的典型案例. 最后，本文对现有研究存在的不足及困难进行了总结和讨论，并进一步展望了未来的发展方向和潜在挑战.
关键词：挥发份；大地电磁测深；地磁测深；岩石物理实验；电导率
doi：10.19975/j.dqyxx.2025-005　　**中图分类号：**P318　　**文献标识码：**A

A review of studies combining natural-source electromagnetic soundings and petrophysical experiments to constrain the volatile distribution in the deep earth

Zhou Hongli[1,2], Li Xin[1*], Deng Yangfan[1*], Zhu Sheng[1,2]
1 State Key Laboratory of Deep Earth Processes and Resource, Guangzhou Institute of Geochemistry, Chinese Academy of Sciences, Guangzhou 510640, China
2 College of Earth and Planetary Sciences, University of Chinese Academy of Sciences, Beijing 100049, China

Abstract: Volatiles (such as H_2O, CO_2) are the crucial factors controlling the physical-chemical properties and dynamic processes of the multi-layer system within the Earth, and therein play an important role in plate tectonics, magmatic-mineral activities, and even the development of the planet's habitable environment. Because volatiles can drastically alter the physical characteristics of crust-mantle rocks, the primary method for determining their content and distribution within the Earth is to combine geophysical observations with high-temperature and high-pressure petrophysical experiments. Of the many physical properties, electrical conductivity is particularly sensitive to the presence and abundance of trace amounts of volatile materials, and therefore the deep conductivity structure de-

收稿日期：2025-01-18；**录用日期：**2025-04-02
基金项目：国家自然科学基金资助项目（92479204，U24A20602）；国家重点研发计划项目（2022YFF0801003）；中国科学院战略性先导科技专项（XDA0430203）
Supported by the National Natural Science Foundation of China (Grant Nos. 92479204, U24A20602), National Key R&D Program of China (Grant No. 2022YFF0801003), and Strategic Priority Research Program of Chinese Academy of Sciences (Grant No. XDA0430203)
第一作者：周虹利，女，在读硕士研究生，主要从事火山区深部结构研究. E-mail：zhouhongli@gig.ac.cn
***通信作者：**李鑫，男，副研究员，主要从事壳幔电性结构与动力学研究. E-mail：lixin@gig.ac.cn
邓阳凡，男，研究员，主要从事壳幔结构探测研究. E-mail：yangfandeng@gig.ac.cn

rived from natural-source electromagnetic (EM) sounding methods such as magnetotellurics (MT) and geomagnetic depth sounding (GDS) offers crucial observational information for constraining the distribution of volatiles in the crust and mantle. This review firstly summarizes the basic principles and characteristics of the major natural-source EM sounding methods, and presents in detail the high-temperature and high-pressure experimental studies on the electrical conductivity of major minerals/rocks and melts in the crust and mantle, then reviews typical cases combining the two methods to study the distribution of deep volatiles in different geological settings. Finally, this review synthesizes and discusses the existing shortcomings and difficulties of current research, and further prospects the future development directions and potential challenges.

Keywords: volatiles; magnetotellurics; geomagnetic depth sounding; petrophysical experiment; electrical conductivity

0　引　言

挥发份包括 Goldschmidt 元素地球化学分类中的亲气元素（氢、碳、氮和惰性气体）及各种化合物，是地球孕育生命的必备因素，是行星宜居性研究的关键. 挥发份在地表环境下多以气态或液态形式存在，并主要富集在大气圈和水圈中（纪伟强和吴福元，2022）. 然而，地球表面只含有地球总挥发份的一小部分，大部分挥发份元素以不同形式储存在地球内部（Pearson et al., 2014; Schmandt et al., 2014）. 例如，碳在还原环境下以金刚石、石墨等形式存在于地球深部，而在氧化环境下则以碳酸盐矿物、含碳熔流体等形式存在（Pearson et al., 2014; Schmidt and Poli, 2013; 徐义刚等, 2024）. 挥发份主要通过俯冲过程进入地球内部，然后经洋中脊、大陆裂谷、地幔柱等途径返回到地球表层系统，整个循环伴随各个圈层之间的相互作用（纪伟强和吴福元, 2022; Kasting and Catling, 2003）（图 1）. 尽管挥发份在地球总质量中所占比例极小，但却强烈影响地球内部岩石的物理-化学性质. 壳幔中的挥发份（H_2O、CO_2 等）可以显著降低岩石的熔点及强度，改变岩石的熔融状态和流变性质，进而影响物质能量循环、岩浆活动及板块构造等动力学过程（Key et al., 2013）. 因此，厘清地球内部的挥发份分布及含量不仅是研究地球内部多圈层系统动态过程及运行机制的关键把手，同时对理解构造-岩浆-成矿作

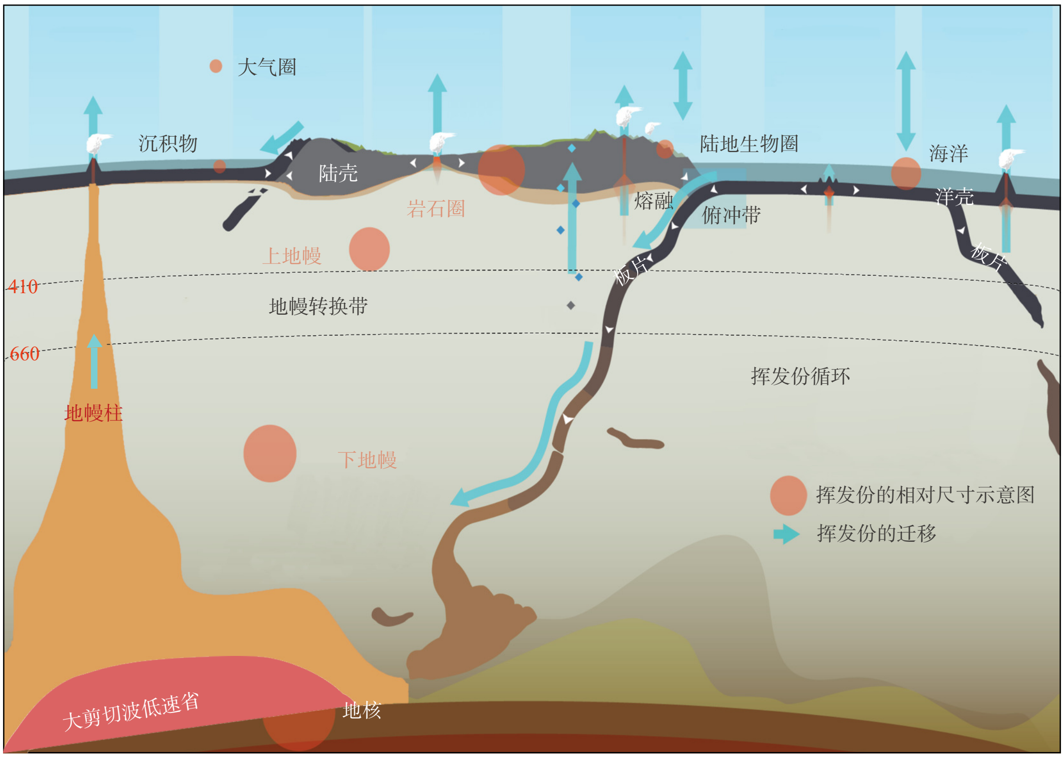

图 1　地球挥发份的分布与循环过程（修改自 Josh Wood 个人主页）

Fig. 1　The distribution and cycling processes of Earth's volatiles (modified from Josh Wood personal website)

用乃至地球宜居环境演化等关键科学问题至关重要，具有重要的科学价值和现实意义.

挥发份含量的直接测量可通过天然深源岩石样品的实验分析来实现（Deines, 2002; Iddon and Edmonds, 2020; Saunders et al., 2012）. 例如，二次离子质谱法或傅里叶变换红外光谱法可用于检测捕掳体中的羟基缺陷，从而评估地幔中的水含量（Xia et al., 2017）. 然而，由于水从地幔运输至地表的过程中会发生脱气作用，因此直接测量样品的水含量可能会低估原位地幔的含水量（Demouchy 2010; Fullea, 2017; Zhao et al., 2019）. 此外，由于岩石样品的覆盖稀疏，且源区深度通常较浅，并不是所有的地幔层位都得到了很好的采样，这就导致了空间分布上的局限性. 另一种挥发份含量的直接测量方式是通过分析高温高压条件下天然或合成样品的挥发份饱和度（Zhao et al., 2004）. 这种利用岩石物理实验模拟的方式可以更接近地球内部原位的物理环境，但获取的结果是矿物能容纳的挥发份最大含量，存在一定程度的高估（Fullea, 2017）.

由于挥发份会影响壳幔岩石的物理属性，如增大电导率，降低剪切波速度，增加地震波的衰减，改变界面形态及性质，因此利用地球物理探测获取深部介质的物理参数结构（波速、密度、电导率等）为约束挥发份空间分布提供了一种间接手段. 在诸多地球物理方法中，以大地电磁测深（magnetotellurics, MT）、地磁测深（geomagnetic deep sounding, GDS）为代表的天然源电磁测深方法具有探测深度大、对微量挥发份敏感的特性，是当前约束地球深部挥发份分布的一种关键地球物理手段. 地球内部电导率取决于岩石的矿物组合、温压条件以及挥发份含量等，其中挥发份含量变化带来的影响尤为重要. 前人针对挥发份元素（主要为 C、H、O）对壳幔主要矿物/岩石及熔体电导率的影响已开展了大量高温高压实验研究（Karato and Wang, 2013; Pommier, 2014; Zhang and Xia, 2021）. 上述研究表明，水的存在会显著提升地幔主要矿物（橄榄石、瓦兹利石、林伍德石等）的电导率（Karato et al., 2020; Yoshino and Katsura, 2012），而当熔体中存在挥发份（如 H_2O 和 CO_2）时，熔体电导率会进一步显著增大（Ni et al., 2011; Sifré et al., 2014）. 因此，联合天然源电磁测深与岩石物理实验结果，为地球内部挥发份含量分布的定量化研究提供了一种有效途径.

本文第 1 节概述了天然源电磁方法的基本原理，分析了不同天然电磁场源在地球深部探测研究中的应用；第 2 节详细回顾了已开展的不同壳幔矿物的电导率实验结果，探讨了不同矿物组分和温压条件对岩石电导率的影响；第 3 节总结了几种用于计算岩石体电导率的多相混合模型；在第 4 节中，通过总结几种典型地质构造背景下的研究案例特点，展示了实际应用中关于熔流体与挥发份研究的发展. 最后，第 5 节对现有研究进行了总结，并展望了未来在壳幔挥发份分布研究领域中可能的发展方向和面临的挑战.

1　天然源电磁测深方法基本原理及特性

天然源电磁测深方法是一类利用地球外部不同场源探测地球内部电性结构的被动场源地球物理方法. 与人工激发场源相比，天然场源电磁信号具有频带范围宽、周期长、探测深度大等优势. 大地电磁测深和地磁测深是目前常用的两种天然源测深方法（Blake et al., 2016; Tikhonov, 1950; 徐光晶等, 2015）. 20 世纪 50 年代以来，这两类方法被广泛应用于壳幔结构探测研究，在地热资源勘探（Abossie et al., 2023）、矿产资源勘查（Deng et al., 2020; Heinson et al., 2018）、火山岩浆系统研究（Bowles-Martinez and Schultz, 2020; Jenkins et al., 2023）、地震活动构造研究（Zhao et al., 2012）、大陆动力学过程研究（Ma et al., 2024）和海洋地质调查（Chesley et al., 2021; Key et al., 2013）等领域发挥着重要作用.

大地电磁测深方法基于平面波假设，以天然电磁波为场源，通过测量地球表面正交的自然变化电磁场，获取包含地表至上地幔电导率分布信息的转换函数（阻抗张量、倾子等）（Cagniard, 1953; Tikhonov, 1950）. 电磁场分量在笛卡尔坐标系下满足如下关系式：

$$\begin{bmatrix} E_x \\ E_y \end{bmatrix} = \begin{bmatrix} Z_{xx} & Z_{xy} \\ Z_{yx} & Z_{yy} \end{bmatrix} \begin{bmatrix} H_x \\ H_y \end{bmatrix} \tag{1}$$

$$[H_z] = \begin{bmatrix} T_x & T_y \end{bmatrix} \begin{bmatrix} H_x \\ H_y \end{bmatrix} \tag{2}$$

其中，Z 和 T 分别表示阻抗和倾子，视电阻率可以通过阻抗计算：

$$\rho_{ij} = \frac{1}{\omega\mu_0}|Z_{ij}|^2 \tag{3}$$

其中，ω表示角频率，μ_0表示磁导率.

相比于 MT，GDS 方法可以探测到更深部的地

幔信息. GDS 方法的场源为地球磁层内的环状电流，传统上通常用假设二次磁场满足一阶带谐函数 $P_1^0=\cos\vartheta_d$ 项描述，利用地磁观测获得有效周期范围在 10^5～10^7 s（数天至数年）之间的 C 响应（Kuvshinov and Semenov, 2012; Olsen, 1998; Schmucker, 1964）:

$$C(\omega,r_a)=-\frac{a\tan\vartheta_d}{2}\frac{H_r(r_a,\omega)}{H_{\vartheta_d}(r_a,\omega)} \tag{4}$$

其中，r_a 为球面坐标系下地磁台站空间位置，ω 为频率，ϑ_d 是观测点的地磁余纬度，H_r 和 H_{ϑ_d} 分别是磁场的径向和水平（指向地磁南）分量.

此外，太阳静日变化（solar quiet daily variation, Sq）也可以被用于探测地幔电性结构. Sq 地磁信号来源于太阳辐射在电离层 E 区（距离地表约 110 km）引起的漩涡电流体系（Schmucker, 1964），包含了丰富的上地幔-地幔过渡带电性结构信息. 相对于 MT 和 GDS 方法的场源，Sq 成像所利用的电离层涡旋电流场源的空间结构更为复杂，且随时间会发生明显变化，因此开展相关成像研究的难度相对更大.

天然源电磁测深方法的探测深度与电磁信号周期直接相关，周期越长，探测深度越深（图 2）. MT 信号的最大周期通常位于数千至数万秒之间，其最大有效探测深度局限于地壳或上地幔，而 GDS 的周期要更长，可达数百天，根据电磁场传播的趋肤效应，其探测范围可以达到下地幔的深度（Kelbert et al., 2008, 2009）. 用于开展 GDS 成像的观测数据主要来源于全球地磁台网和少量卫星观测，其时间序列可能长达几十年（Kelbert et al., 2009; Kuvshinov and Semenov, 2012; Olsen, 1998; Püthe et al., 2015）. MT 信号主要反映岩石圈电性结构信息，GDS 信号则主要是对地幔过渡带及下地幔的电性结构敏感，而 Sq 信号恰好可以弥补二者之间的观测空白区.

2　矿物岩石电导率实验结果

2.1　壳幔常见矿物电导率

地球内部不同深度的岩石矿物组分和物理性质

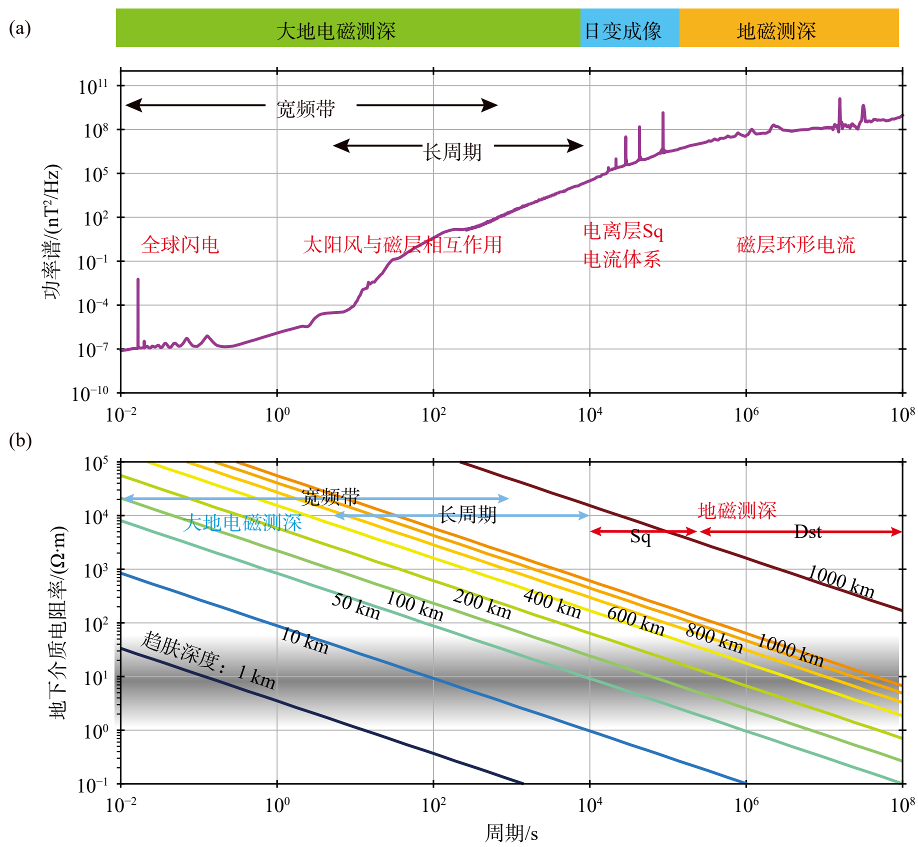

图 2　（a）不同周期范围地球天然磁场功率谱（数据来源 Constable and Constable, 2023）;（b）不同周期范围对应的电磁成像方法及理论趋肤深度，其中黑色阴影区大致对应活动火山深部电阻率范围区间

Fig. 2　(a) Power spectra of the Earth's natural magnetic field in different period ranges (data from Constable and Constable, 2023); (b) Corresponding electromagnetic imaging methods and theoretical skin depths for different period ranges, with the black shaded area roughly corresponding to the resistivity range of active volcanoes at depth

存在显著差异. 大陆地壳主要由富硅富铝的长英质岩石（如花岗岩和片麻岩）组成；大洋地壳主要由镁铁质岩石（如玄武岩和辉长岩）组成；而上地幔主要由超镁铁质橄榄岩组成. 不同岩石的电导率相差较大（图 3），因此电导率结构可以作为区分地球内部岩石组分的有效参数.

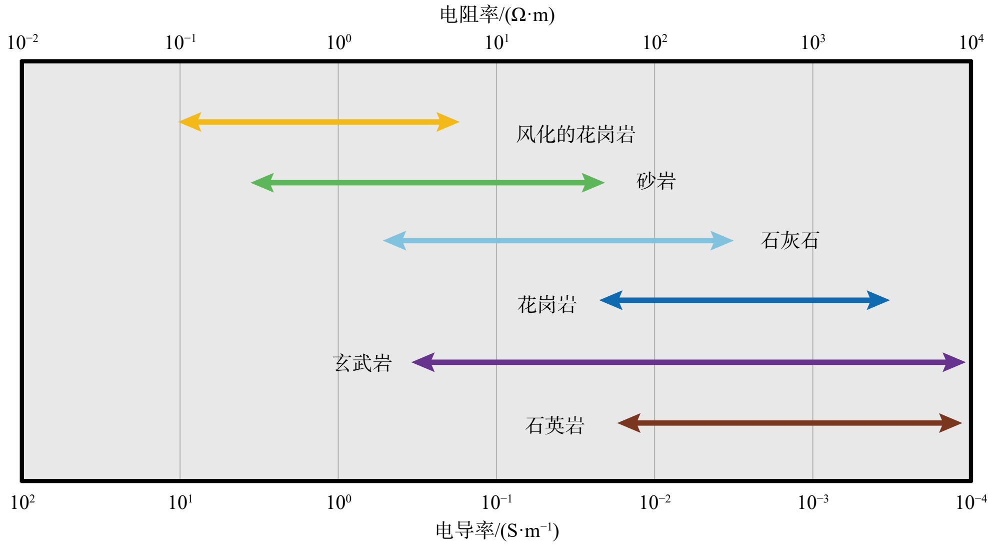

图 3　地壳常见岩石电导率分布（数据来源 Comeau, 2015）

Fig. 3　Electrical conductivity distribution of common rocks in the crust (data from Comeau, 2015)

前人在实验室环境下测量了不同温压条件下常见地壳矿物的电导率（图 4a），结果显示温度是影响这些矿物电导率的一个主要因素（Guo et al., 2011; Selway, 2019; Wang et al., 2010; Yang, 2012）. 基于上述观测，Hashim 等（2013）给出了地壳岩石电导率随温度变化的经验表达式：

$$\rho_c = \exp\left(-\ln 2.9 + \frac{8581.8}{T+273}\right) \tag{5}$$

针对地幔的主要矿物，前人同样开展了大量的高温高压电导率测量（Gardés et al., 2014; Wang et al., 2006; 杨晓志, 2014; Yoshino et al., 2009）（图 4b-4d）. 橄榄石作为上地幔的主要成岩矿物，许多研究测量了其在不同温度、压力条件及含水量的情况下的导电性质（Dai and Karato, 2009; Yoshino and Katsura, 2009, 2012）. 例如，Yoshino 和 Katsura（2009）基于高温高压实验建立了含水橄榄石的电导率模型：

$$\sigma = 10^{4.73}\exp\left(\frac{-223}{RT}\right) + 10^{2.98}\exp\left(\frac{-165}{RT}\right) + 10^{1.9}C_w\exp\left(-\frac{88.7-0.16C_w^{1/3}}{RT}\right) \tag{6}$$

其中，C_w是指岩石中的水含量，R 是通用气体常数（J mol^{-1} K^{-1}），T 为温度（K）.

Yoshino 和 Katsura（2012）的研究中得到的瓦兹利石电导率模型：

$$\sigma = 10^{2.46}\exp\left(\frac{-140}{RT}\right) + 10^{1.40}C_w\exp\left(-\frac{80.0-0.02C_w^{1/3}}{RT}\right) \tag{7}$$

林伍德石的电导率模型在不同温度条件下具有一定差别，其电导率表示为（Yoshino and Katsura, 2009）：

$$\sigma = 10^{1.44}C_w\exp\left(-\frac{108-0.67C_w^{1/3}}{RT}\right) + \sigma_0^{Fe}X_{Fe}\exp\left(-\frac{H_0^{Fe}-\alpha^{Fe}X_{Fe}^{1/3}}{RT}\right) \tag{8}$$

$$T < 1000\ \text{K}:\ \sigma_0^{Fe} = 10^{2.67}\quad H_0^{Fe} = 206\quad \alpha^{Fe} = 2.14$$

$$T > 1000\ \text{K}:\ \sigma_0^{Fe} = 10^{4.0}\quad H_0^{Fe} = 201\quad \alpha^{Fe} = 1.55$$

其中，X_{Fe}是含铁林伍德石中 Fe 的摩尔分数.

2.2　含挥发份熔体电导率

熔体电导率的高低与挥发份的种类与含量密切相关. Ni 等（2011）采用 VET（Vogel-Fulcher-Tammann）方程来描述玄武质熔体电导率与温度和水含量的关系：

$$\log_{10}\sigma = 2.172 - \frac{860.82-204.46\sqrt{w}}{T-1146.8} \tag{9}$$

其中，σ指电导率，单位为 S/m；T 是温度，单位为 K；w 是水含量，单位为 wt.%.

Sifré等（2014）针对上地幔软流圈，在高温高压条件下对具有不同含量 H_2O 和 CO_2 的玄武岩进

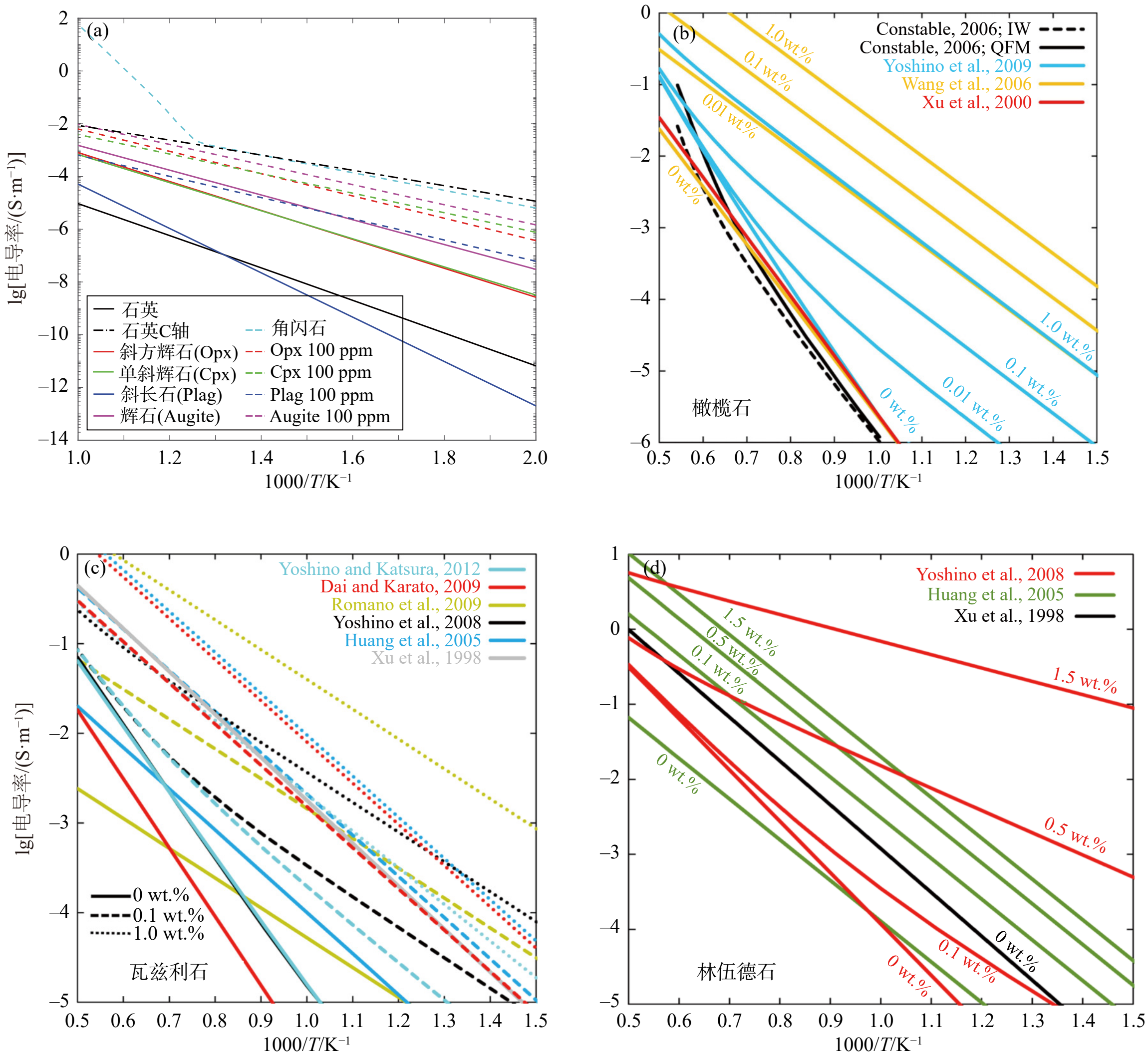

图 4　（a）常见地壳矿物电导率随温度的变化（引自 Selway, 2019）：在随机取向的多晶集合体中，石英电导率测量数据来源于 Bagdassarov 和 Delépine（2004）；沿着 C 轴取向的石英数据来自 Wang 等（2010）；斜方辉石（Opx）数据来源于由 Yang 等（2012）研究；单斜辉石（Cpx）数据来源于 Yang 等（2011）；斜长石（Plag）数据来源于 Yang 等（2012）报告；富铁辉石（Augite）数据来源于 Yang 和 McCammon（2012）；角闪石相关的研究数据则由 Wang 等（2012）提供；不同研究中各种岩石的电导率作为温度与含水量的函数：（b）橄榄石；（c）瓦兹利石；（d）林伍德石（引自 Zhang and Xia, 2021）

Fig. 4　(a) Electrical conductivity of common crustal minerals as a function of temperature (from Selway, 2019): quartz measured in a randomly oriented polycrystalline aggregate (Bagdassarov and Delépine, 2004) and along the C-axis (Wang et al., 2010), orthopyroxene (Opx) (Yang et al., 2012), clinopyroxene (Cpx) (Yang et al., 2011), plagioclase (Plag) (Yang et al., 2012), iron-rich augite (Yang and McCammon, 2012), and amphibole (Wang et al., 2012); Electrical conductivity of three different rocks as a function of temperature and water content in various studies: (b) olivine; (c) wadsleyite; (d) ringwoodite (from Zhang and Xia, 2021)

行实验测量（图 5），在证明结果不会受脱气的影响下，建立了一个同时考虑 H_2O 和 CO_2 对玄武质熔体电导率影响的半经验模型：

$$\sigma_{\mathrm{model}} = \sigma^{H_2O} + \sigma^{CO_2} = \sigma_0^{H_2O} \exp\left(\frac{-E_a^{H_2O}}{RT}\right) + \sigma_0^{CO_2} \exp\left(\frac{-E_a^{CO_2}}{RT}\right) \tag{10}$$

其中，σ_0、E_a 分别指含水硅酸盐与碳酸盐的 Arrhenius 定律电导率指前因子和活化能项.

电导率指前因子 σ_0 取决于熔体成分、含量和压力 P，因此需要在实验室中对样品进行测定获得相应的关系（Samrock et al., 2021）. 实验室温度在 810℃～1 400℃、压强在 0.5～1.0 GPa 之间，含有 60.79 wt.% 的安山岩熔体电导率为（Guo et al., 2017）：

$$\log_{10}\sigma = 5.23 - 0.56\omega^{0.6} - \frac{8130.4 - 1462.7\omega^{0.6} + (581.3 - 12.7\omega^2)P}{T} \tag{11}$$

实验室温度在 595℃～1 393℃、压强在 0.5～

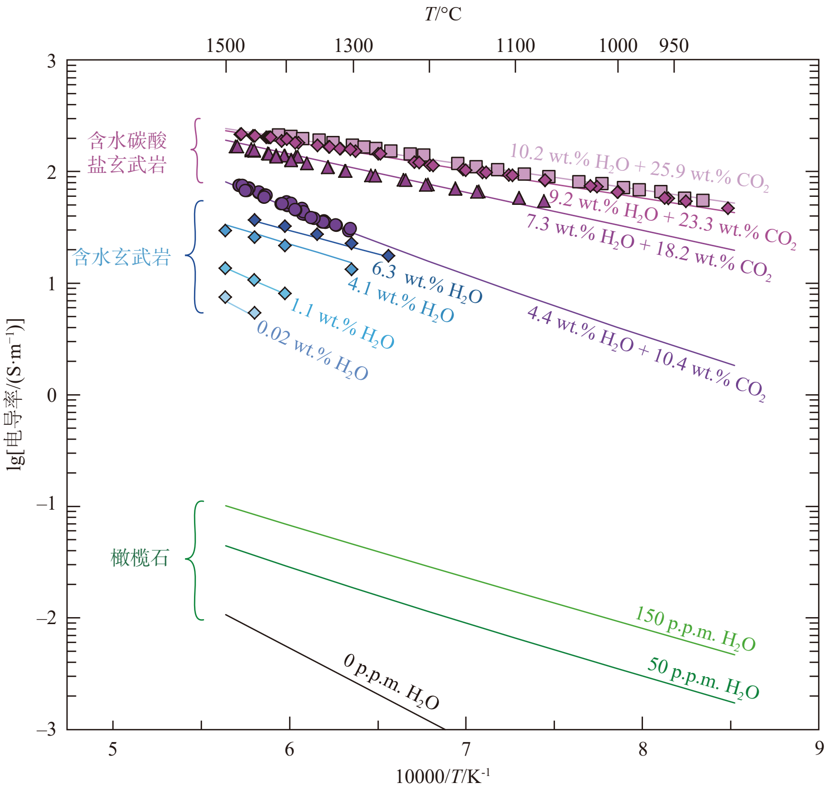

图 5　不同温度条件下含 H_2O、CO_2 玄武质熔体和橄榄石电导率实验室测量结果（引自 Sifré et al., 2014）

Fig. 5　Electrical conductivity of carbonated basaltic melt and olivine with H_2O and CO_2 under different temperature conditions from laboratory measurements (from Sifré et al., 2014)

1.0 GPa 之间，含有 75.72 wt.% 的流纹岩熔体电导率为（Guo et al., 2016）：

$$\log_{10}\sigma = 2.983 - 0.0732\omega - \frac{3528 - 233.8\omega + (763 - 7.5\omega^2)P}{T} \quad (12)$$

式（11、12）中，ω代表熔体中的溶解水含量，单位是 wt.%. 压强 P 的单位是 GPa，温度 T 的单位是 K.

实验室温度为 1 573℃，压强在 0.7～2.9 GPa 之间，含有 65.8 wt.% 的辉长岩熔体电导率为（Laumonier et al., 2019）：

$$\sigma = \exp\left[(0.395\omega + 4.65) + p\cdot(-1.77\mathrm{e}-6\omega + 3.91\mathrm{e}-5) - \frac{1}{RT}(60000 + 0.645P)\right] \quad (13)$$

其中，压强 P 的单位是 bar，温度 T 的单位是 K.

上述三种熔体的电导率经验公式也适用于压强小于 0.5 GPa 的低压环境，可用于探讨地壳中的熔体问题（Guo et al., 2016, 2017）.

2.3　含盐水流体的电导率

实验室测量含盐流体的电导率研究表明（Quist and Marshall, 1969），当温度和压强到达一定程度时，含盐流体的电导率会出现急剧下降的现象（图 6a），这与超临界条件下地热流体的部分特征类似（Kummerow et al., 2020）.

基于高温-高压实验室结果（Guo and Keppler, 2019; Klumbach and Keppler, 2020; Sinmyo and Keppler, 2017），Sinmyo 和 Keppler（2017）给出了一种描述含盐水流体电导率随温度、压力和 NaCl 浓度变化的经验公式：

$$\log_{10}\sigma = A + B/T + C\log_{10}c + D\log_{10}\rho + \log_{10}\Lambda_0 \quad (14)$$

其中，σ是电导率，单位是 S/m；T 是温度，单位是 K；c 是 NaCl 的浓度，单位是 wt.%；ρ是纯水的密度，单位是g/cm^3；A、B、C、D 将通过最小二乘回归方法由实验测量结果确定. Guo 和 Keppler（2019）研究了 5 GPa 超高压下 NaCl 溶液的电导率经验公式：

$$\log_{10}\sigma_f = -0.919 - \frac{827.5}{T} + 0.852\log_{10}c + 7.61\log_{10}\gamma(T,P) + \log_{10}\Lambda_0(T,\gamma) \quad (15)$$

其中，σ_f是挥发份电导率，$\gamma(T,P)$是在一定的温压条件下的纯水密度，$\Lambda_0(T,\gamma)$是 NaCl 在水中无限稀释时的摩尔电导率. 此外，Klumbach 和 Keppler（2020）研究了压强小于 1 GPa 时含 HCl 的流体：

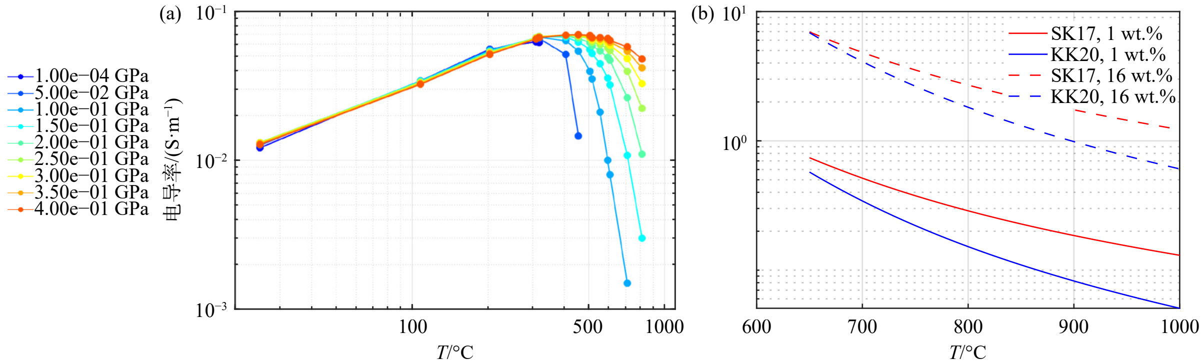

图 6　不同温压条件下含盐水流体的电导率.（a）温度在 25 ℃～812 ℃，压力为 1.00e-04～4.00e-01 GPa 范围内 NaCl 溶液（0.01 mol/L）的电导率（引自 Quist and Marshall, 1969; Samrock et al., 2021）;（b）利用 Sinmyo 和 Keppler（2017）（SK17）和 Klumbach 和 Keppler（2020）（KK20）测定的在 1 wt.% 和 16 wt.%HCl 浓度时流体挥发份的电阻率（数据来自 Cordell et al., 2022）

Fig. 6　(a) Electrical conductivity of NaCl solutions (0.01 mol/L) within temperatures ranging from 25 ℃ to 812 ℃ and pressures from 1.00e-04 to 4.00e-01 GPa (from Quist and Marshall, 1969; Samrock et al., 2021); (b) Electrical resistivity of fluid volatiles at 1 wt.% and 16 wt.% HCl concentrations, as determined by Sinmyo and Keppler (2017) (SK17) and Klumbach and Keppler (2020) (KK20) (data from Cordell et al., 2022)

$$\log_{10}\sigma_{\mathrm{f}} = -2.032 - \frac{205.8}{T} + 0.895\log_{10}\alpha + 3.89\log_{10}\gamma(T,P) + \log_{10}\Gamma_0(T,\gamma) \tag{16}$$

其中，α是 HCl 的浓度，$\Gamma_0(T,\gamma)$是 HCl 的极限摩尔电导率.

流体的电导率与温度和压强均有关，式（15、16）还加入了对溶质的考虑，通常在流体中还可能存在如 NaCl、HCl 等卤素气体或溶解金属，有助于形成含盐热液，并与成矿作用有关（Afanasyev et al., 2018; Cordell et al., 2022）. 因此可以用端元极值作为分析的前提，不同端元的结果间相差约一个数量级，然而，当温度较低时，两种不同方法间的结果相差不大（图 6b）.

3　岩石电导率的多相混合模型

3.1　两相混合模型

实验室测量最早把岩石简化为固体和含水流体两相，提出了经典的两相混合的 Archie 定律（Archie, 1942）. 该定律建立在一定的假设上：岩石是由固体基质和填充其中的单一性质流体组成，是一种均匀空隙介质，且主要由孔隙中的流体导电，不考虑其他的导电因素，如导电黏土矿物. Archie 定律现已被广泛应用（Glover et al., 2000; Glover, 2010; Weitemeyer et al., 2011），被表示为：

$$\sigma = C\sigma_{\mathrm{f}}\Phi^{-m} \tag{17}$$

其中，σ是体电导率，C 是经验常数（接近 1），σ_{f}是流体电导率，Φ是流体的体积分数，m 是流体的连通性参数（图 7a），其中 m 在 1～1.3 之间代表连通良好，m=2 表示连通性较差.

随着有关熔体的实验室研究发展，发现 Archie 定律在部分熔融矿物岩石的研究中发挥了新的作用，实验室中的测量结果表明，原本认定为非导电硅酸盐的矿物在高温条件下转变为半导体，因此提出了修正后的广义 Archie 定律（Glover et al., 2000; Ten Grotenhuis et al., 2005）：

$$\sigma = \sigma_{\mathrm{m}}(1-\Phi)^{p} + \sigma_{\mathrm{f}}\Phi^{m} \tag{18}$$

其中：

$$p = \frac{\log_{10}(1-\Phi^{m})}{\log_{10}(1-\Phi)} \tag{19}$$

式中σ_{m}是固体基质的电导率，m、p 分别表示流体和岩石固体的连通性参数.

除了 Archie 定律，Hashin-Shtrikman 有界模型也可以表示两相混合模型（图 7c）：

$$\sigma_{\mathrm{HS}}^{+} = \sigma_{\mathrm{f}}\left[1 - \frac{3(1-\Phi)(\sigma_{\mathrm{f}}-\sigma_{\mathrm{m}})}{3\sigma_{\mathrm{f}} - \Phi(\sigma_{\mathrm{f}}-\sigma_{\mathrm{m}})}\right] \tag{20}$$

$$\sigma_{\mathrm{HS}}^{-} = \sigma_{\mathrm{m}}\left[1 + \frac{3\Phi(\sigma_{\mathrm{f}}-\sigma_{\mathrm{m}})}{3\sigma_{\mathrm{m}} + (1-\Phi)(\sigma_{\mathrm{f}}-\sigma_{\mathrm{m}})}\right] \tag{21}$$

其中σ_{HS}^{+}和σ_{HS}^{-}分别表示不同情况下电导率的上限与下限（图 7b）.

使用 Archie 定律的前提条件是已知各相的电导率，其中熔体的导电性受其载流子的迁移率控制. 实验室得到的半经验模型如下（Pommier and Le-Trong, 2011）：

$$\sigma = \sigma_0\exp\left(-\frac{E_{\mathrm{a}} + P\Delta V}{RT}\right) \tag{22}$$

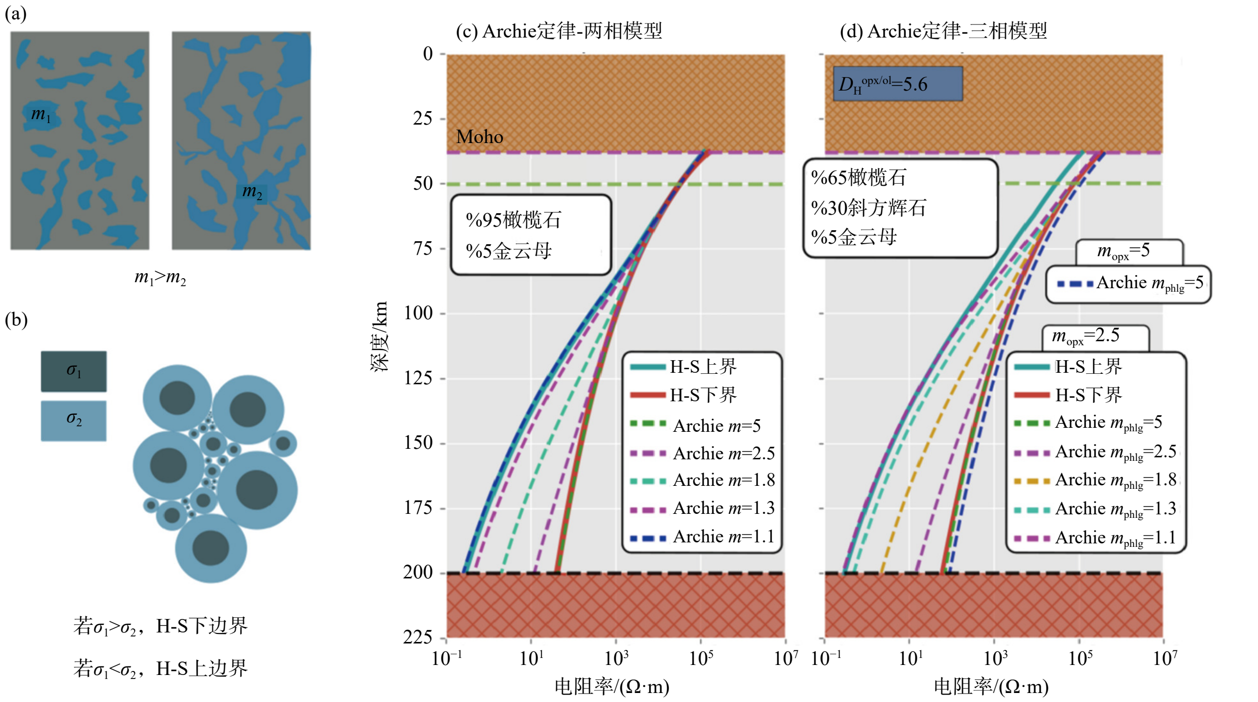

图 7　Archie 定律概念理解图.（a）广义 Archie 定律中连通性指数 m 的含义；（b）Hashin-Shtrikman 边界；（c）不同连通指数 m 下，两相混合金云母-橄榄石电导率变化；（d）不同连通指数 m 下，三相混合金云母-橄榄石-斜方辉石电导率变化（引自Özaydin and Selway, 2020）

Fig. 7　Sketches showing the conceptual understanding of (a) the phase exponent m in the generalized Archie's law and (b) Hashin-Shtrikman bounds. Graphs demonstrating the conductivity of (c) a phlogopite-olivine mixture with phlogopite having varying values of m for a two-phase assemblage; (d) a phlogopite-olivine-orthopyroxene mixture with phlogopite having varying values of m for a three-phase assemblage (from Özaydin and Selway, 2020)

式中，σ_0是电导率指前因子，即材料本身的电导率，E_a为活化能，R为气体常数（8.314 3 J mol^{-1}K^{-1}），ΔV为活化体积（cm^3 mol^{-1}），T为温度（K），P为压力（1 MPa = 10^6 Pa）.

3.2　三相混合模型

针对饱和挥发份岩浆系统，简单的固体、熔体两相无法描述复杂的系统，需要进一步考虑挥发份在系统中起到的作用. 在岩浆系统中，岩浆挥发份是不可忽视的一部分. 在岩浆上升过程中，会释放出 H_2O 和 CO_2，并可能伴随冷却结晶（Newman and Lowenstern, 2002）. 岩浆经历减压或冷却结晶，熔体可能会达到饱和状态，进而产生出溶的挥发份，该状态下出现固体、熔体和挥发份三种相态. 三相岩浆系统的体电导率σ_{bulk}可以采用广义 Archie 定律（Glover, 2010）（图 7d）：

$$\sigma_{\text{bulk}} = \sum_{i=1}^{n} \sigma_i \phi_i^{m_i} \tag{23}$$

其中，σ_i是各相的电导率，ϕ_i是体积分数，m_i是连通性参数，需要满足连通性守恒条件：

$$\phi_{\text{f}}^{m_{\text{f}}} + \phi_{\text{melt}}^{m_{\text{melt}}} + \phi_{\text{c}}^{m_{\text{c}}} = 1 \tag{24}$$

其中，m_{f}、m_{c}、m_{melt}分别为挥发份、固体、熔体相的连通性参数. 通常固体连通性参数作为体积分数的函数进行计算，以满足连通性守恒（Glover, 2010）. 此外，利用端元值计算，可以获得最大和最小的体积电阻率，以更好地限制饱和系统中各相的影响（Cordell et al., 2022）.

在考虑了熔体、温度和挥发份含量之间的热力学耦合关系后，Samrock 等（2021）通过热力学建模将地球物理学和岩石学观测数据联系起来，比如，利用岩浆系统热力学建模软件 Rhyolite-MELTS，可以建立不同温压条件和给定岩石组分的热力学相平衡关系（图 8），再结合三相系统来估计熔体以及挥发份的含量，发现在系统达到高度结晶时，挥发相的含量可达 5 vol.%.

4　典型研究案例

4.1　活动造山带

造山带是地壳或岩石圈挤压缩短所造成的强烈构造变形带（郑永飞等，2015）. 由印度大陆和欧

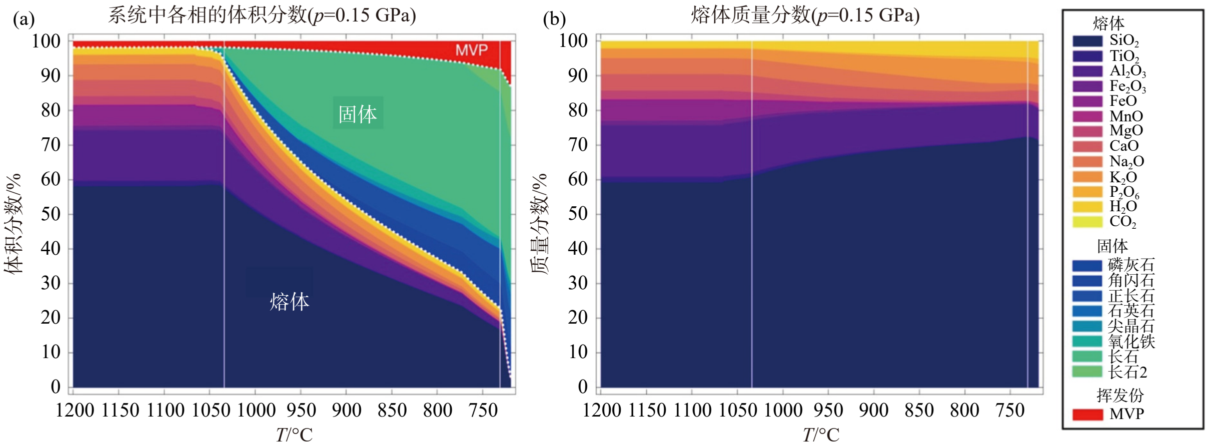

图 8　利用 Rhyolite-MELTS 估计的结晶过程中的熔体、固体和岩浆挥发份（magmatic volatile phase, MVP）的组成与体积分数.（a）系统内各相的体积分数；（b）安山岩熔体模型及各成分的含量（引自 Samrock et al., 2021）

Fig. 8　Melt, solid and magmatic volatiles phase (MVP) composition and fractions during the course of crystallization as predicted by Rhyolite-MELTS, (a) system volume fractions and (b) weight fractions within the melt phase only (from Samrock et al., 2021)

亚大陆的碰撞、挤压形成的青藏高原—喜马拉雅造山带是目前地球上最大最显著的陆-陆碰撞造山带. 自 20 世纪 90 年代起，国内外学者在青藏高原及邻区开展了大量 MT 深部探测研究，为揭示高原壳幔结构与组成提供了关键的观测资料（Bai et al., 2010; Chen et al., 1996; Dong et al., 2020; Li X et al., 2020; Rippe and Unsworth, 2010; Sun et al., 2003; Unsworth et al., 2004, 2005; Wang et al., 2014; Wei et al., 2001; Zhao et al., 2012）. 这些研究在高原的中下地壳深度探测到广泛发育的低阻异常层，并推断含盐水流体、部分熔融或二者的共同作用是导致低阻异常的主要成因. 前人在假定熔/流体电阻率的前提下，根据上述观测得到的中下地壳电阻率值，利用简单的 Archie 定律估算了熔/流体的含量. 例如，Unsworth 等（2005）根据实验观测，假定纯熔体的电阻率值为 0.1～0.3 Ω·m，并在假设熔体之间具有很好的连通性的前提下，估算了藏南地区中下地壳存在 5%～14% 的部分熔融；在藏东的 MT 观测研究中，Bai 等（2010）则假定深部熔/流体的电阻率为 0.05～0.20 Ω·m，并据此估算了中下地壳的流体含量（图 9）. 上述类似的方法被广泛用于估算青藏高原及其它活动造山带地壳深部的流体分布（Bai et al., 2010; Dong et al., 2016; Rippe and Unsworth, 2010; Xue et al., 2021）. 然而，需要指出的是，该类方法仍存在一些明显的不足. 首先，熔/流体的电阻率值由组分、温度、压力等一系列因素控制，因此无法采用固定范围的电阻率值套用到所有情况，而需要根据具体情况分析. 其次，含熔/流体岩石的电阻率值还与熔/流体的几何分布及连通程度密切相关，而传统的 Archie 定律难以充分反映这一复杂性. 最后，水的存在不仅会显著降低地壳岩石的熔点，促进部分熔融，同时也能降低熔体的电阻率，而这些研究普遍忽略了水含量对电阻率的影响.

为提升对深部熔/流体含量的约束能力，近几年开展的一些研究针对上述问题采取了一系列措施. 例如，Chen 等（2018）针对熔体电导率会随环境变化的问题，在实验室特定温压条件下，测量了从研究区深部获取的地壳岩石熔体的电导率，进而与大地电磁成像结果对比，推测了喜马拉雅山西北部地壳高导体可以解释为 4%～16% 的富水熔体（图 10）. Dong 等（2020）在考虑了温压条件以及 Archie 定律中不同参数对计算结果的影响，在前人对研究区得出的深部地壳的温度、压强以及最大含水量条件的基础下，利用 Guo X 等（2018）实验得到的含水花岗岩电导率公式，估计熔体以及水含量. Sheng 等（2021）除了使用前文的方法估算熔体电导率外，还在电导率的基础上进一步利用 HS+边界条件等方法估计温度，其中通过密度估算的压力，为估计熔体分数与水含量提供了更加准确的约束条件.

4.2　活动大洋俯冲带

在两个岩石圈板块相向运动过程中，俯冲作用导致一个板块俯冲到另一个板块之下，形成俯冲带. 根据俯冲板片的性质，可以将俯冲带分为大洋俯冲带与大陆俯冲带两类（Stern 2002; 张泽明等, 2020; Zheng and Chen, 2016）. 在大洋俯冲带中，板片释放的水以流体、含水熔体或超临界流体形式迁移到地幔楔中，对周围地幔的物理化学性质产生重

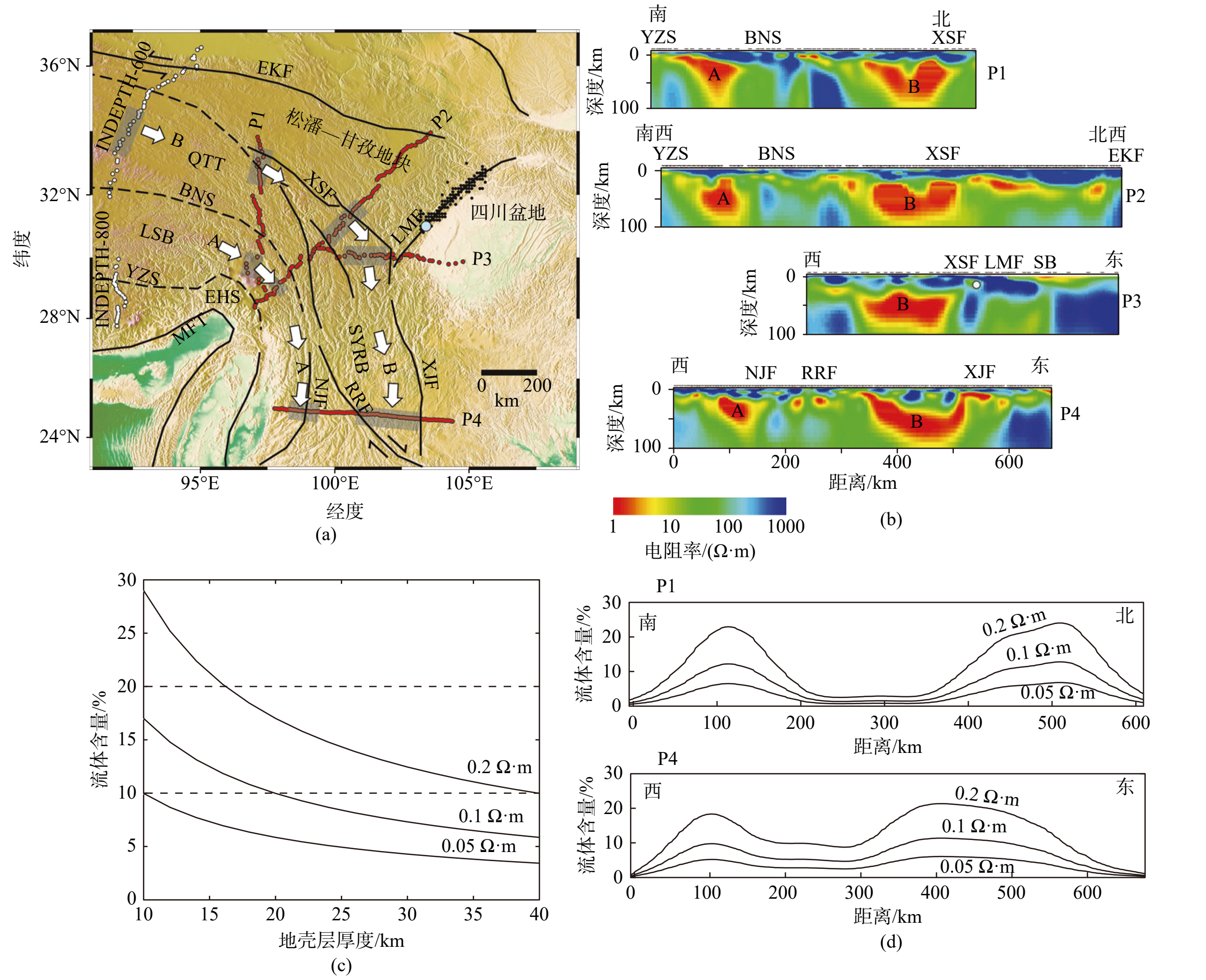

图 9　（a）青藏高原东部及邻近区域地质构造简图；（b）青藏高原东部的大地电磁测深电阻率垂直剖面；（c）不同厚度地壳高导层（电导值固定为 10000 S）对应的流体含量；（d）P1 和 P4 剖面中下地壳（厚度假定为 20 km）电导值对应的流体含量（引自 Bai et al., 2010）

Fig. 9　(a) Map showing surface relief of the eastern Qinghai–Xizang Plateau and the adjacent area; (b) Electrical resistivity cross-sections for eastern Qinghai–Xizang Plateau; (c) Variation of thickness and fluid content (porosity) for a crustal layer with a conductance of 10000 S; (d) Fluid content (porosity) of a 20-km-thick mid-crustal layer required to account for the conductance of profiles P1 and P4 (from Bai et al., 2010)

要影响（Hermann et al., 2006; Manning, 2004; Zheng et al., 2011）. 这些挥发份的迁移对于岩浆弧的形成和元素循环具有关键作用，因此俯冲带岛弧火山比洋中脊和洋岛火山更容易富集挥发份. 俯冲带不仅是物质和能量交换的关键区域（Wilson et al., 2014），还与火山活动密切相关. 地球动力学结果认为地幔楔和俯冲板片顶部的温度可以达到脱水熔融的温度（Johnson and Plank, 2000; Syracuse et al., 2010; Van Keken et al., 2002），导致俯冲板片携带的挥发份对地球深部的熔融行为和流体迁移造成显著影响（张泽明等，2020）. 其中，从俯冲板片释放的含水流体向上迁移，可以控制岩浆弧的生成和元素循环（Hermann et al., 2006; Huang et al., 2021; Wannamaker et al., 2009; Yang et al., 2025），改造岩石圈地幔（Deng et al., 2021; Zhu et al., 2024），并形成火山（Zhao et al., 2021）.

MT 方法凭借其对熔/流体的敏感性，通常用于示踪熔/流体的分布（Garcia et al., 2015; 韩江涛等, 2019; Mu et al., 2022; Ni et al., 2011）. Wannamaker 等（2009）根据新西兰 Marlborough 地区 MT 观测获取了深部电阻率剖面，发现俯冲带上覆地壳和上地幔中存在五个低阻异常体，被解释为俯冲板片在不同深度脱水释放、向上迁移的流体（图 11a）；Worzewski 等（2011）利用 MT 观测结果研究 Costa 至 120 km 深度的俯冲带水化和脱水循环过程；Egbert 等（2022）利用了宽频带和长周期 MT 观测结果，推测 Cascadia 弧前区流体的分布，发现流体在板块上方的变质沉积岩中积累，而镁铁质岩石则

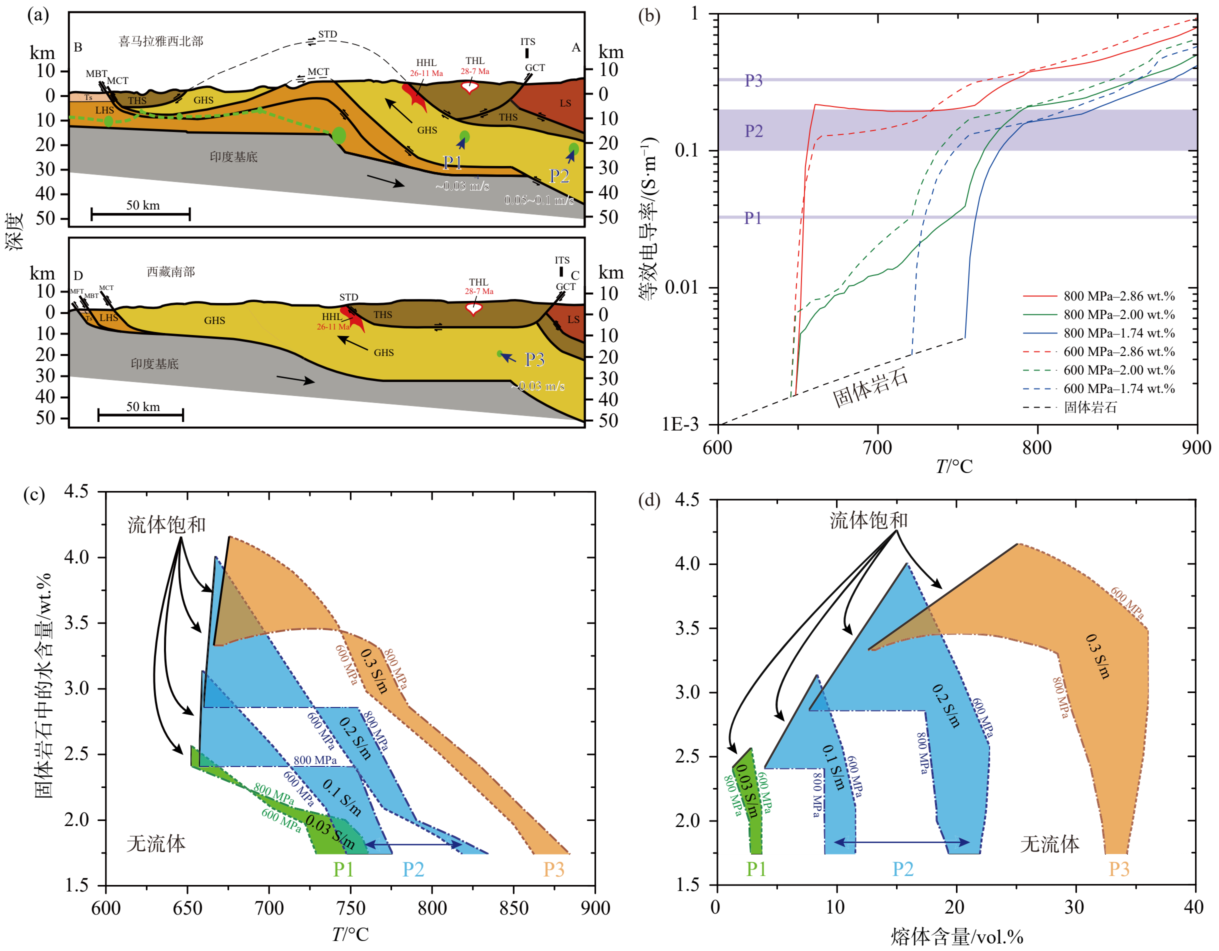

图 10　（a）喜马拉雅山西北部和藏南的简化地质剖面图；（b）等效电导率与温度的关系，黑色虚线表示固体岩石开始熔融，P1-3 指示三个不同位置的观测电导率异常值；（c, d）固体岩石中的水含量与温度及熔体含量的关系，黑色实线表示无流体和流体饱和的边界（引自 Chen et al., 2018）

Fig. 10　(a) Simplified geological profile of the northwestern Himalayas and southern Xizang; (b) The relationship between effective electrical conductivity and temperature, with the black dashed line indicating the onset of solid rock melting and P1-3 representing three types of conductivity anomalies; (c, d) The relationship between water content in solid rock and temperature and melt content, with the black solid line indicating the boundary between no fluid and fluid saturation (from Chen et al., 2018)

相对干燥；Chesley 等（2021）在 Hikurangi 陆缘北段进行了海底电磁探测，研究中针对水含量的问题，基于修正后的 Archie 定律估算了该区域的孔隙度. Huang 等（2021）测量了含有少量含盐水流体的橄榄石的电导率，并系统整理了全球不同俯冲带地幔楔高导异常值分布，为估计弧前地幔楔中流体的含量提供了约束（图 11b）.

4.3　板内火山区

地球上的大多数火山活动发生在板块边界，可以用经典的板块构造理论解释. 然而，也有许多在大陆板块内部，远离板块边界的火山通常被归因于各种局部的构造作用（Ball et al., 2021）. 例如大陆区域，岩石圈可能会发生局部裂谷作用，导致其伸展和减薄，从而使软流圈热物质上涌并发生减压熔融（Mckenzie and Bickle, 1988）；当热的、低密度的地幔柱从下地幔上升时，也会发生减压熔化（Campbell and Griffiths, 1990）；此外，岩石圈与地幔柱的相互作用、岩石圈下小规模的地幔对流作用等都可能会导致板内火山的形成（陈克非等, 2023; Rooney et al., 2007; Schilling et al., 1992; Zhang et al., 2024）. 一般来说，火山活动生成的岩浆体积和火山喷发速率会受到地幔温度、挥发份含量及其挥发速率的调节（Brune et al., 2023; White and Mckenzie, 1989）.

MT 方法是探测活动/休眠火山深部岩浆系统的有力工具（Aivazpourporgou et al., 2015; Bedrosian et al., 2018; Comeau, 2015; Cordell et al., 2018; Hübert et al., 2018）. 火山区域的岩浆通道系统会受到如岩浆从地幔上涌并在地壳底部积累，或构造应

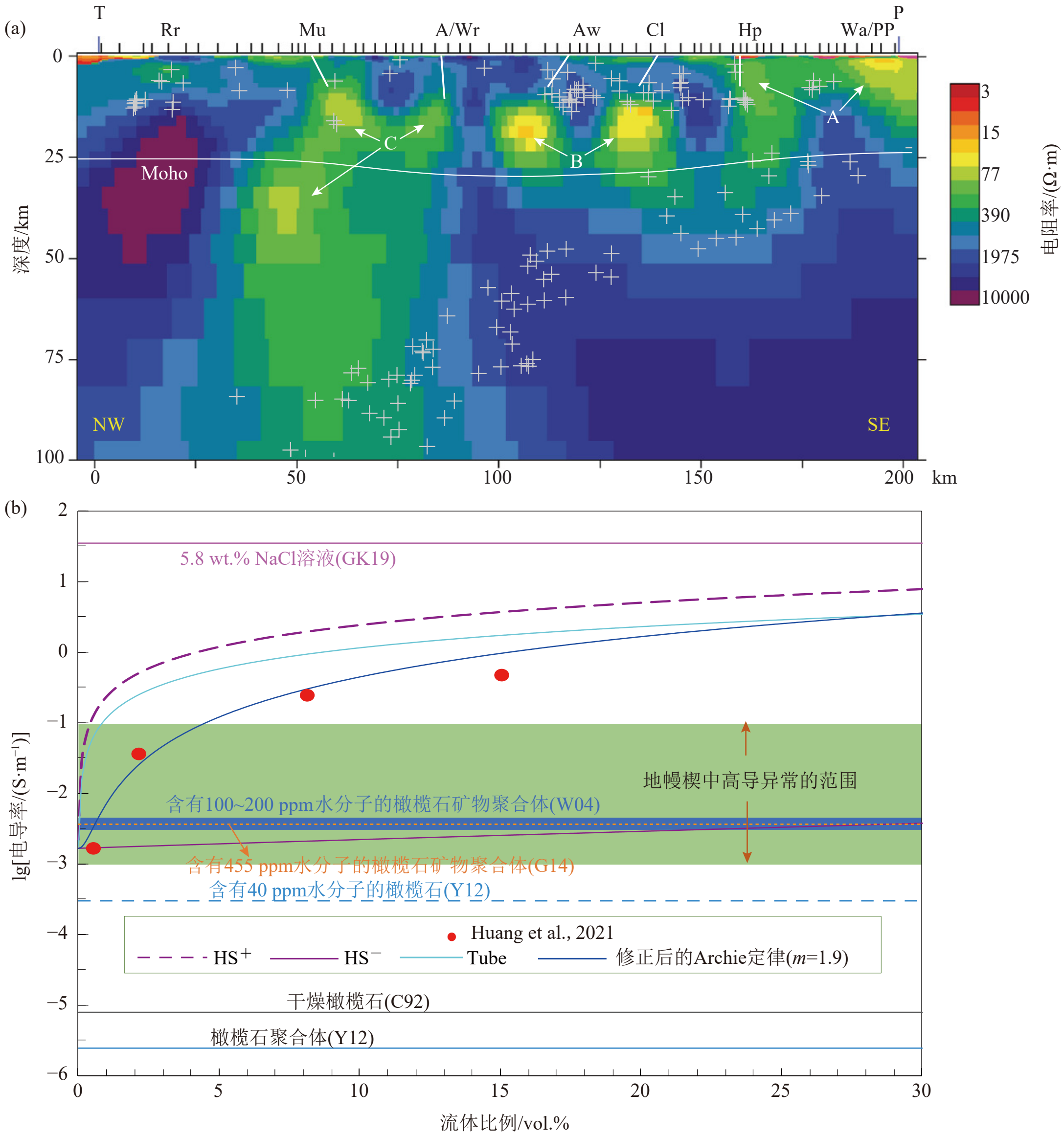

图 11　（a）新西兰 Marlborough 地区俯冲带 MT 电阻率剖面，其中“+”表示在大地电磁剖面上，叠加在 25 km 条带上的地震活动（引自 Wannamaker et al., 2009）；（b）镁橄榄石电导率与含盐水流体比例的关系（引自 Huang et al., 2021）

Fig. 11　(a) Nonlinear 2D inversion model of electrical resistivity below the Marlborough–northern Westland district. Seismicity ("+" symbols) is superposed for a 25-km swath along the magnetotelluric transects (from Wannamaker et al., 2009); (b) The relationship between the electrical conductivity of forsterite (magnesium-rich olivine) and the proportion of saline aqueous fluid (from Huang et al., 2021)

力加载的影响，发生几何形状的变化（Johnson et al., 2008; Li et al., 2021; Liu et al., 2021; Valentine and Perry, 2007）. 三维大地电磁成像结果能够有效地揭示岩浆储库的空间分布和熔融状态（Comeau et al., 2016; Gao et al., 2020; Li et al., 2024; Peacock et al., 2015; Unsworth and Rondenay, 2013）.

Bowles-Martine 和 Schultz（2020）采用 MT 方法研究了 Newberry 火山的结构和岩浆组成，探测到一个 3～5 km 深度的岩浆储层，并用 8%～11% 的部分熔融解释. 中国东北地区广泛分布着板内火山作用（赵凌强等，2024），其中 Li S 等（2020）根据中国东北新生代火山群长周期大地电磁观测，发现岩石圈高电阻背景中存在局部低电阻异常，这些异常与地表的新生代火山部分重合，结合岩石物理模拟结果，利用 HS 模型计算出火山下方低阻异常体的熔体含量在 2%～15% 之间，并根据橄榄石的电导率模型（Gardés et al., 2014）估计出水含量约为 400 ppm. 由于这些局部异常体均起源于上地幔深部的环状低阻异常，因此前人推测太平洋俯冲板片脱水导致的热物质上涌可能是导致东北地区大规模新生代火山活动的原因（Guo Z et al., 2018; Li et al., 2021; Tang et al., 2014）. 在五大连池火山区，

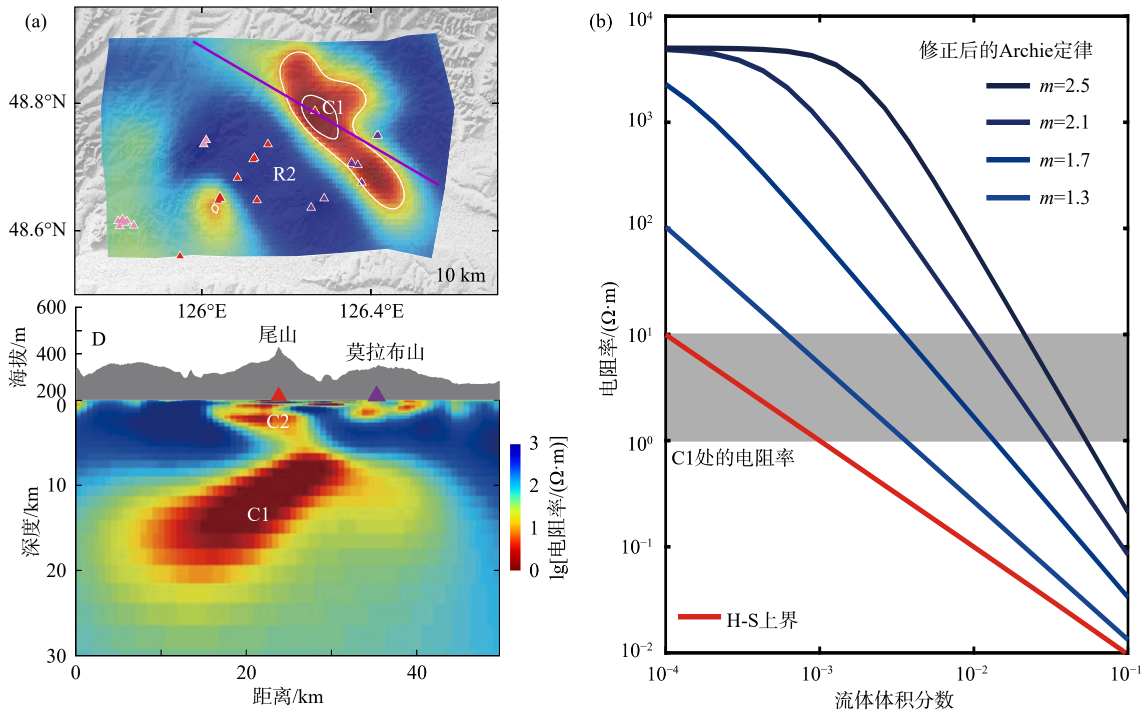

图 12　（a）五大连池火山 MT 成像结果；（b）电阻率与含盐流体体积分数的关系（引自 Sun et al., 2023）

Fig. 12　(a) MT imaging results of the Wudalianchi volcanic field; (b) Bulk resistivity as a function of fluid volume fraction (from Sun et al., 2023)

Sun 等（2023）基于大地电磁观测结果（图 12a），利用修正后的 Archie 定律计算具有不同含量含盐水流体的地壳岩石电阻率值（图 12b），推测低阻异常体反映了富水挥发份物质沿着上地壳薄弱带（断层）上升.

4.4　稳定克拉通地区

克拉通是大陆地壳中包含陆核的古老且稳定区域. 克拉通的显著特点包括地壳长期稳定、地震和火山活动少、地温梯度低、密度小、黏度高等. 因其可以保存大陆地区复杂的生长和演化历史，克拉通成为国内外研究岩石圈结构及其演化的焦点地区（Artemieva and Mooney, 2001; 胡祥云等, 2020）. 稳定的克拉通核部存在的巨厚岩石圈根，在大地电磁成像结果中通常呈现为高电阻率特征（Jones et al., 2013; Spratt et al., 2014; Yang et al., 2025）. 例如，北美 Rae 克拉通具有巨厚的高电阻率岩石圈地幔，并呈现从北东到西南方向逐渐增加的趋势. 这种变化特征可能与地幔温度轻微升高或地幔水含量增加有关（Evans et al., 2005; Spratt et al., 2014）.

大地电磁研究结果中还发现，在一些克拉通岩石圈内存在显著的电性不连续现象，局部岩石圈地幔会出现大范围的高导体. 这些高导异常通常用名义无水矿物中的氢、颗粒边界薄的石墨膜或铁的存在来解释（Jones and Ferguson, 2001; Jones et al., 2003; Selway, 2014; Selway et al., 2014）. 北美 Slave 克拉通是世界上最小的太古宙稳定克拉通单元，大地电磁研究发现其中部的岩石圈地幔存在高导异常区，Jones 等（2003）将其解释为石墨膜的影响. 然而，近期 Bettac 等（2023）在三维 MT 反演结果中发现 Slave 克拉通中央岩石圈存在的高导异常可以用金云母和含水的碳酸盐岩熔体来解释，他们进一步结合实验室岩石物理研究结果，在假设地幔岩石组分的条件下，估算出地幔中的含水量（图 13）. 澳大利亚南部的 Gawlery 克拉通中部地幔也存在明显的高导异常，Maier 等（2007）推测此处异常是名义上无水矿物中氢含量的增加与石墨膜共同作用的结果，而 Thiel 和 Heinson（2013）则认为部分电导率的增加可能来源于颗粒边界的硫化铁.

4.5　软流圈

岩石圈是地幔具有较高强度且不易发生化学变化的区域，覆盖在较弱且活跃的软流圈之上. 岩石圈-软流圈边界（lithosphere asthenosphere boundary, LAB）是地球内部刚性岩石圈和黏塑性软流圈之间的分界面. 虽然该界面在传统的热模型中被定义为平缓的热边界层（Parker and Oldenburg, 1973），

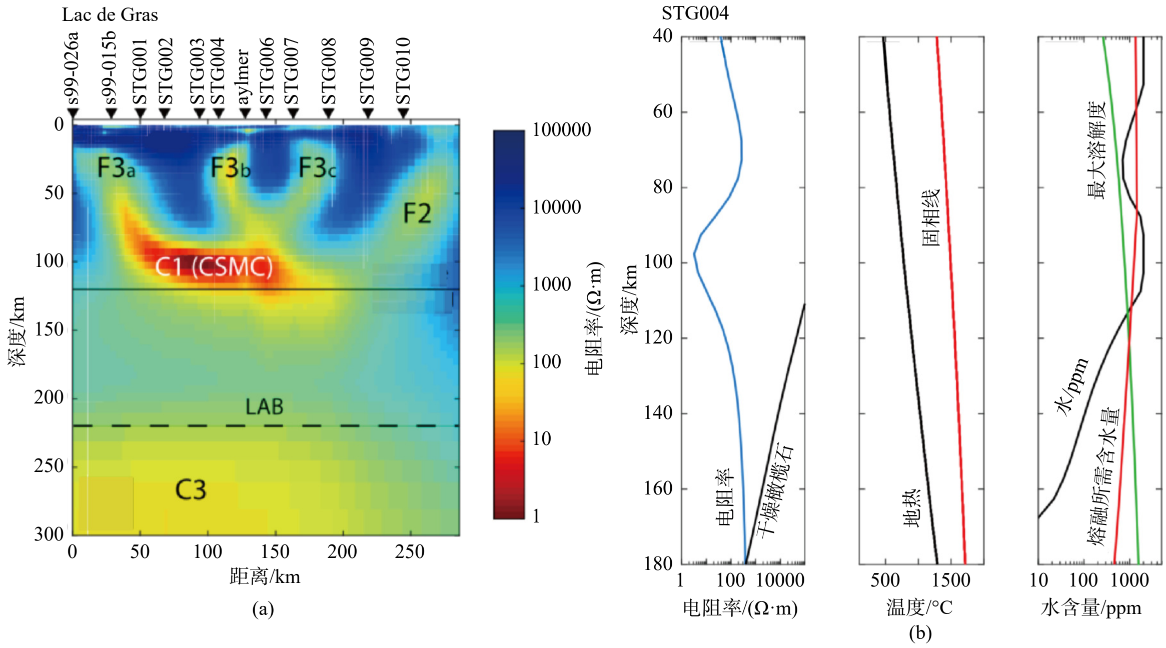

图 13　（a）Slave 克拉通的代表性电阻率剖面之一；（b）使用 Rippe 等（2013）的方法，估计 Slave 克拉通中央高导体的含水量（引自 Bettac et al., 2023）

Fig. 13　(a) Model results are shown as one of representative resistivity profiles across the Slave Craton; (b) Using the method of Rippe et al. (2013), the water content of the central conductor in the Slave Craton is estimated (from Bettac et al., 2023)

但近年来的研究显示软流圈表现出了异常物理性质，如地震速度突然发生跳跃性变化（Fischer et al., 2020; Rychert and Harmon, 2018; Rychert et al., 2020）、LAB 底部的低速层（Forsyth et al., 1998; Harmon et al., 2020）、低电阻率层（Baba et al., 2006; Key et al., 2013; Naif et al., 2013; Wang et al., 2020）. 对于这些异常的成因，人们提出了多种可能性，其中含水（Karato, 2012; Wang et al., 2006）和部分熔融（Yoshino et al., 2006）是其中最具有代表性的两种解释.

地幔中的部分熔融问题涉及多重因素，由于 LAB 深度的温度环境不足以产生大量硅酸盐熔体来满足所观测到的结果，所以仅靠部分熔融无法解释 LAB 特征（Hier-Majumder and Courtier, 2011）；而名义不含水矿物（NAMs）中的水则无法解释软流圈地幔电导率在某些区域存在的各向异性，且水饱和状态下的橄榄石也不足以解释高导现象（黄晓葛等，2017）. 挥发份（如 H_2O 和 CO_2）在地幔中的存在会显著降低固相温度，促进部分熔融的产生（Kawakatsu et al., 2009），在软流圈低温且干燥的区域，碳酸盐熔体会相对稳定呈现出高电导率，但当温度升高或 H_2O 含量增加时，熔体会转变为碳酸盐玄武岩（Dasgupta et al., 2013; Hirschmann, 2010）. Sifré等（2014）测量了含挥发份（CO_2 和 H_2O）的玄武质熔体的电导率，进一步探讨了部分熔融机制在 LAB 中的作用.

MT 成像结果中显示了 LAB 上方岩石圈通常表现出低电导性，而软流圈表现出高导电性（Kawakatsu and Utada, 2017）. Naif 等（2013）在 Nicaragua 海的 Cocos 板块获取的海底电磁大地成像结果中发现在 45～70 km 深度具有明显的高电导层，并将其解释为一个被上覆低渗透率盖层封闭的部分熔融层. 以往的研究多采用如 HS 混合模型来估计两相混合系统的电导率，而忽略了挥发份的影响. 对含水地幔电导率计算通常仅考虑水对固相线的影响，忽略了 CO_2 的贡献，这导致橄榄岩熔融温度被高估（Dasgupta et al., 2013），实际上即使是微量的 CO_2 也足以在 LAB 处引发熔融.

Blatter 等（2022）将含挥发份的地幔熔融实验结果，与大地电磁观测相结合，约束了 Cocos 板片 LAB 的性质，认为 Cocos 板片下方的高导异常需要用中等至异常高的熔体分数和挥发份含量来解释. 地幔电阻率是与岩石成分、温度、系统水含量、熔体分数和 CO_2 含量相关的复杂函数（图 14），之所以 LAB 的熔体和挥发份的含量存在很大的不确定性，主要原因是温度的不确定性，Blatter 等（2022）在固定了水含量且限制 CO_2 的基础上，推测 Cocos 板片下方的部分高导异常为富含挥发份的熔体通道，并估计出熔体分数为 1～3 vol.%. 地幔柱可以在 LAB 通道中聚集富含挥发份的熔体，

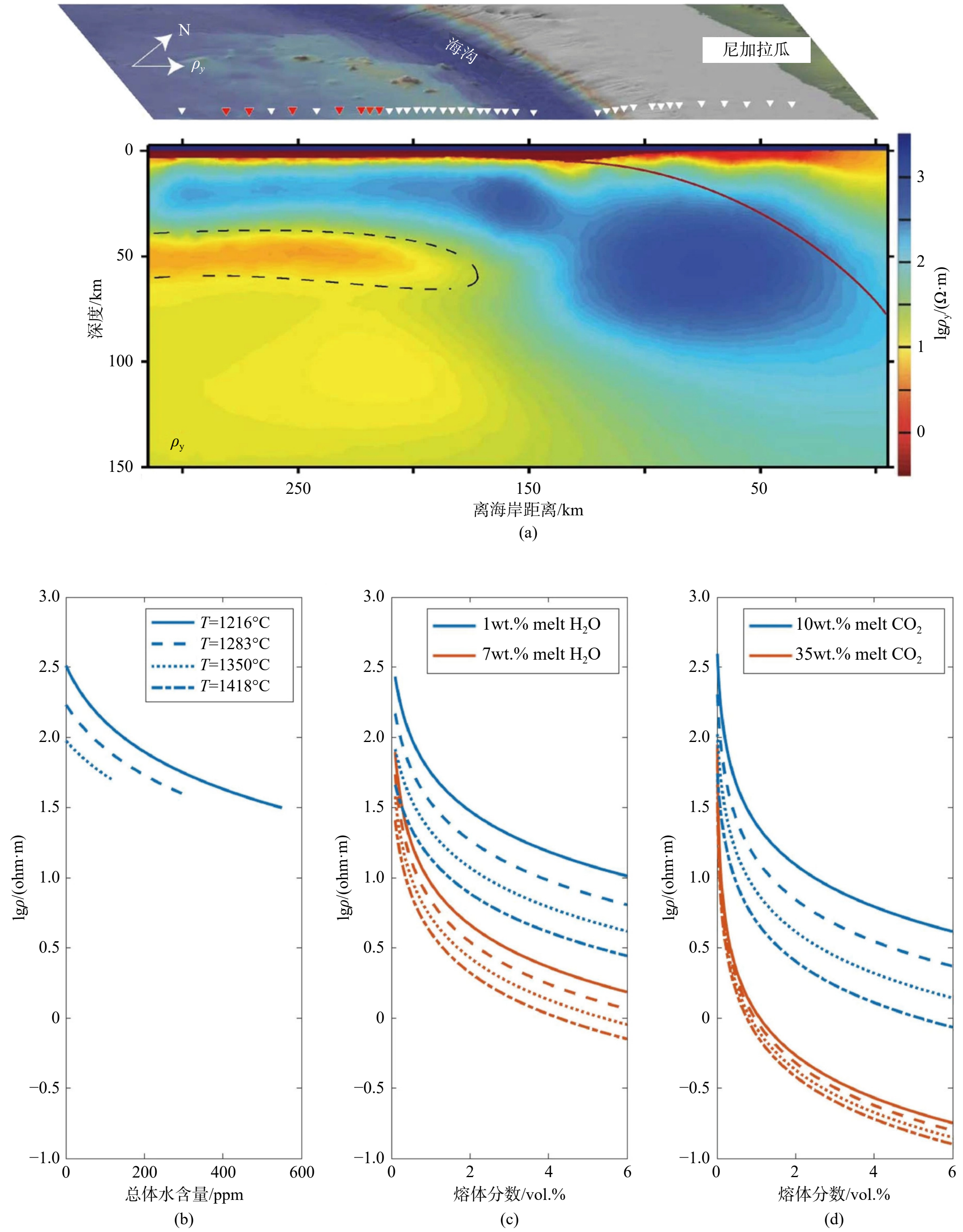

图 14　（a）美洲中部 Cocos 大洋板块岩石圈-软流圈电阻率结构；（b-d）温度、水含量、熔体分数和熔体挥发份（H_2O、CO_2）含量对地幔体电阻率的影响（引自 Blatter et al., 2022）

Fig. 14　(a) Resistivity structure near the Cocos Plate LAB; (b-d) Effects of temperature, water content, melt fraction, and melt volatile (H_2O, CO_2) content on the resistivity of the mantle (from Blatter et al., 2022)

因此推断 Cocos 板片下方富含挥发份的熔体，可能与 Cocos 板片附近未被检测到的地幔柱有关（Mehouachi and Singh, 2018; Wang et al., 2020）.

4.6　全球地幔过渡带

地幔是地球内部重要的水储库. 尽管以橄榄石为主的浅层地幔储水能力有限，但橄榄石高压相的储水能力很强，地幔过渡带可能储存相当于几个现今海洋的水（Karato et al., 2020; Pearson et al., 2014）. 目前估计地幔过渡带含水量主要通过高温高压下水饱和的实验测量，但不同研究所获得的含量具有较大的不一致性（黄晓葛等，2017），水含量测

量结果从接近饱和（1.0～2.0 wt.%）到基本干燥（<0.1 wt.%）均有估计（Dai and Karato, 2009; Karato, 2011; Kuvshinov, 2012; Yoshino et al., 2008a; Yoshino and Katsura, 2009）. Huang 等（2005）首次测量了含水瓦兹利石、林伍德石的电导率，推测地幔过渡带是含水的，Dai 和 Karato（2009）的研究也支持了富水的观点. Yoshino 等（2008b）的研究中则提出相对干燥的瓦兹利石和尖晶橄榄石模型可以用于解释部分大洋与大陆板块下的地幔过渡带电导率剖面结果.

深部电导率探测为地幔过渡带水含量估计提供了另外一种途径. 近年来许多研究使用 GDS 方法来获得高分辨率地幔电导率结构，进而约束地幔过渡带水含量. Kelbert 等（2008）引入了一种基于非线性共轭梯度的三维反演方法生成了全球地幔三维电导率模型，随后许多三维反演算法被提出，并不断被改进（Kuvshinov and Semenov, 2012; Sun et al., 2015）. Li S 等（2020）提出了一种新的三维 GDS 反演方法，提高了数据利用率和反演结果的可靠性，构建了更为真实的电导率模型. Zhang 等（2022）利用电离层场源模型，对全球 127 个站点的地磁数据进行反演，估算地幔过渡带的平均含水量仅为 0.03 wt.%（图 15）. Zhang 等（2023）利用日变数据和 *C* 响应进行联合反演，结果显示全球地幔过渡带近乎干燥. 然而，结合地球化学对岩石中的水溶解度分析以及地震与电导率观测结果，Khan 和 Shankland（2012）认为环太平洋（尤其是东亚）地幔过渡带水含量较高，而太平洋西北部与中南部相对较低；在 Munch 等（2020）利用 GDS 反演得到的全球电导率模型中，显示出欧洲地区的地幔过渡带含水量低、而北美和东北亚比较高的特点.

5　总结与展望

本文较为系统地回顾了利用天然场源电磁测深与高温高压岩石物理实验观测联合约束地球深部挥发份（主要为 CO_2 和 H_2O）分布的原理方法，以及在一些构造背景下的典型应用案例. 由于挥发份的加入会显著降低壳幔矿物及熔体的电导率，利用大地电磁或地磁测深方法可以探测到不同构造背景（如活动造山带、俯冲带）、不同圈层范围内（中下地壳、岩石圈地幔、软流圈、地幔过渡带等）与挥发份相关的高导异常. 基于上述观测结果，结合矿物/熔体的电导率实验测量资料，可进一步对挥发份的含量进行定量约束. 上述方法为我们获取地球内部挥发份分布提供了关键的观测信息，但是目前仍存在一些局限性，相应的，我们也可以在此基础上发展新的方向：

（1）天然源电磁测深的探测深度范围与场源信号的周期范围密切相关，因此不同的测深方法只能获取特定范围内的电性结构. 例如，大地电磁方法主要对地表至上地幔浅部结构敏感，无法获取深部地幔信息；地磁测深主要对地幔过渡带以下结构敏感，而浅部结构信息的缺失会加剧反演多解性，降低深部成像结果的精确度. 目前来说，开展多种天然电磁场源（平面电磁波、日变及地磁扰动等）的联合反演成像，完整构建地表至深部地幔的电性结构是解决上述问题的有效途径.

（2）天然源电磁成像方法的原理决定了其分

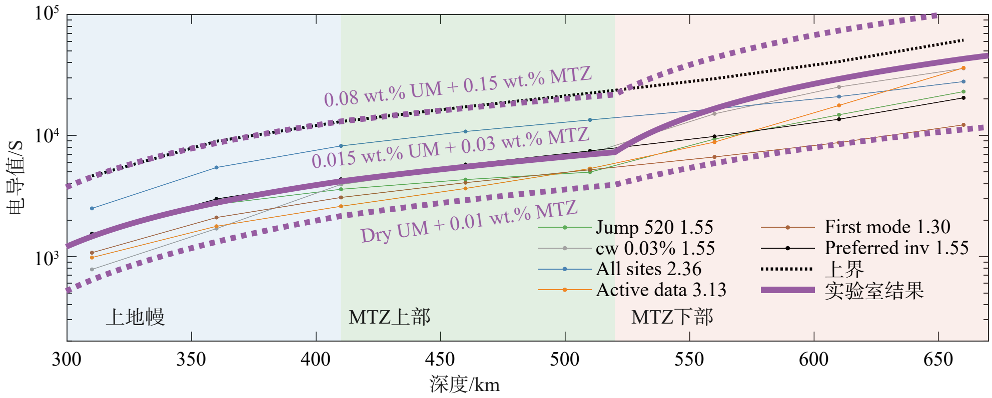

图 15　不同数据和反演方法得到的电导率-深度剖面图，紫色的粗实线是基于实验计算的电导率结果，其中地幔过渡带含水量为 0.03 wt.%（引自 Zhang et al., 2022）

Fig. 15　Conductance-depth profile of plausible inverted models derived from various data and inversion schemes. The thick purple lines denote calculated conductance based on laboratory studies. Water content in the mantle transition zone (MTZ) is 0.03 wt.% (from Zhang et al., 2022)

辨能力随着周期/深度的增大而降低，这严重限制了利用相关观测约束挥发份含量的准确度. 开展天然电磁数据与地震、重力等其他地球物理数据的联合反演不仅可以有效压制反演不确定性和多解性（Ma et al., 2025; Moorkamp et al., 2011），提升成像结果的准确度和分辨率，而且可以为约束挥发份含量提供额外的物理参数信息（波速、密度等）.

（3）地幔岩石电导率主要受到挥发份含量、温度和熔体比例的控制，而这些变量在热力学上应该是相互关联的. 然而，传统方法往往忽略了这些变量之间的热力学相平衡关系，导致经常会得到违背物理定律的估算结果（Blatter et al., 2022; Cordell et al., 2022）. 为了更加准确地约束挥发份含量，可以通过 Melts、PerpleX 等工具引入针对不同温压条件、岩石类型的热力学均衡模型，计算出热力学均衡状态下的矿物/熔体组合及挥发份比例.

致谢

感谢审稿人和编辑提供的建设性意见和建议. 感谢 GIG-Geophysics Lab 团队成员给予的帮助.

References

Abossie A, Fisseha S, Abebe B. 2023. Crustal resistivity structures beneath the western flank across the Central Main Ethiopian Rift: Its implications for partial melt and pathways[J]. Journal of Volcanology and Geothermal Research, 441: 11.

Afanasyev A, Blundy J, Melnik O, et al. 2018. Formation of magmatic brine lenses via focussed fluid-flow beneath volcanoes[J]. Earth and Planetary Science Letters, 499: 256-256.

Aivazpourporgou S, Thiel S, Hayman P C, et al. 2015. Decompression melting driving intraplate volcanism in Australia: Evidence from magnetotelluric sounding[J]. Geophysical Research Letters, 42(2): 346-354.

Archie G E. 1942. The electrical resistivity log as an aid in determining some reservoir characteristics[J]. Transactions of the AIME, 146(01): 54-62.

Artemieva I M, Mooney W D. 2001. Thermal thickness and evolution of Precambrian lithosphere: A global study[J]. Journal of Geophysical Research: Solid Earth, 106(B8): 16387-16414.

Baba K, Chave A D, Evans R L, et al. 2006. Mantle dynamics beneath the East Pacific Rise at 17°S: Insights from the Mantle Electromagnetic and Tomography (MELT) experiment[J]. Journal of Geophysical Research: Solid Earth, 111(B2): 18.

Bagdassarov N, Delépine N. 2004. α–β Inversion in quartz from low frequency electrical impedance spectroscopy[J]. Journal of Physics and Chemistry of Solids, 65(8): 1517-1526.

Bai D H, Unsworth M J, Meju M A, et al. 2010. Crustal deformation of the eastern Tibetan Plateau revealed by magnetotelluric imaging[J]. Nature Geoscience, 3(5): 358-362.

Ball P W, White N J, Maclennan J, et al. 2021. Global influence of mantle temperature and plate thickness on intraplate volcanism[J]. Nature Communications, 12(1): 2045.

Bedrosian P A, Peacock J R, Bowles-Martinez E, et al. 2018. Crustal inheritance and a top-down control on arc magmatism at Mount St Helens[J]. Nature Geoscience, 11(11): 865-870.

Bettac S P, Unsworth M J, Pearson D G, et al. 2023. New constraints on the structure and composition of the lithospheric mantle beneath the Slave craton, NW Canada from 3-D magnetotelluric data – Origin of the Central Slave Mantle Conductor and possible evidence for lithospheric scale fluid flow[J]. Tectonophysics, 851: 229760.

Blake S, Henry T, Muller M R, et al. 2016. Understanding hydrothermal circulation patterns at a low-enthalpy thermal spring using audio-magnetotelluric data: A case study from Ireland[J]. Journal of Applied Geophysics, 132: 1-16.

Blatter D, Naif S, Key K, et al. 2022. A plume origin for hydrous melt at the lithosphere-asthenosphere boundary[J]. Nature, 604(7906): 491-494.

Bowles-Martinez E, Schultz A. 2020. Composition of magma and characteristics of the hydrothermal system of Newberry Volcano, Oregon, from magnetotellurics[J]. Geochemistry Geophysics Geosystems, 21(3): 18.

Brune S, Kolawole F, Olive J-A, et al. 2023. Geodynamics of continental rift initiation and evolution[J]. Nature Reviews Earth & Environment, 4(4): 235-253.

Cagniard L. 1953. Basic theory of the magneto-telluric method of geophysical prospecting[J]. Geophysics, 18(3): 605-635.

Campbell I H, Griffiths R W. 1990. Implications of mantle plume structure for the evolution of flood basalts[J]. Earth and Planetary Science Letters, 99(1): 79-93.

Chen J, Gaillard F, Villaros A, et al. 2018. Melting conditions in the modern Tibetan crust since the Miocene[J]. Nature Communications, 9(1): 3515.

Chen K F, Lin Y, Shen W H, et al. 2023. The origin of the Tengchong volcano: A review of geophysical and geochemical studies[J]. Reviews of Geophysics and Planetary Physics, 54(2): 216-230 (in Chinese).

Chen L, Booker J R, Jones A G, et al. 1996. Electrically conductive crust in southern Tibet from INDEPTH magnetotelluric surveying[J]. Science, 274: 1694-1696.

Chesley C, Naif S, Key K, et al. 2021. Fluid-rich subducting topography generates anomalous forearc porosity[J]. Nature, 595 (7866): 255-260.

Comeau M. 2015. Electrical resistivity structure of the altiplano-puna magma body and volcan uturuncu from magnetotelluric data[D]. Netherlands: Delft University of Technology.

Comeau M J, Unsworth M J, Cordell D. 2016. New constraints on the magma distribution and composition beneath Volcán Uturuncu and the southern Bolivian Altiplano from magnetotelluric data[J]. Geosphere, 12(5): 1391-1421.

Constable C, Constable S. 2023. A grand spectrum of the geomagnetic field[J]. Physics of the Earth and Planetary Interiors, 344: 107090.

Cordell D, Unsworth M J, Díaz D. 2018. Imaging the Laguna del Maule Volcanic Field, central Chile using magnetotellurics: Evidence for crustal melt regions laterally-offset from surface vents and lava flows[J]. Earth and Planetary Science Letters, 488: 168-180.

Cordell D, Naif S, Troch J, et al. 2022. Constraining magma reservoir conditions by integrating thermodynamic petrological models and bulk resistivity from magnetotellurics[J]. Geochemistry Geophysics Geosystems, 23(9): 18.

Dai L, Karato S-I. 2009. Electrical conductivity of wadsleyite at high temperatures and high pressures[J]. Earth and Planetary Science Letters, 287(1): 277-283.

Dasgupta R, Mallik A, Tsuno K, et al. 2013. Carbon-dioxide-rich silicate melt in the Earth's upper mantle[J]. Nature, 493(7431): 211-215.

Deines P. 2002. The carbon isotope geochemistry of mantle xenoliths[J]. Earth-Science Reviews, 58(3): 247-278.

Demouchy S. 2010. Diffusion of hydrogen in olivine grain boundaries and implications for the survival of water-rich zones in the Earth's mantle[J]. Earth and Planetary Science Letters, 295(1): 305-313.

Deng J, Yu H, Chen H, et al. 2020. Ore-controlling structures of the Xiangshan volcanic basin, SE China: Revealed from three-dimensional inversion of magnetotelluric data[J]. Ore Geology Reviews, 127: 103807.

Deng Y F, Xu Y G, Chen Y. 2021. Formation mechanism of the north-south gravity lineament in eastern China[J]. Tectonophysics, 818: 9.

Dong H, Wei W, Jin S, et al. 2016. Extensional extrusion: Insights into south-eastward expansion of Tibetan Plateau from magnetotelluric array data[J]. Earth and Planetary Science Letters, 454: 78-85.

Dong H, Wei W, Jin S, et al. 2020. Shaping the surface deformation of central and south Tibetan Plateau: Insights from magnetotelluric array data[J]. Journal of Geophysical Research: Solid Earth, 125(9): e2019JB019206.

Egbert G D, Yang B, Bedrosian P A, et al. 2022. Fluid transport and storage in the Cascadia forearc influenced by overriding plate lithology[J]. Nature Geoscience, 15(8): 677-682.

Evans S, Jones A G, Spratt J, et al. 2005. Central Baffin electromagnetic experiment (CBEX): Mapping the North American Central Plains (NACP) conductivity anomaly in the Canadian arctic[J]. Physics of the Earth and Planetary Interiors, 150(1): 107-122.

Fischer K M, Rychert C A, Dalton C A, et al. 2020. A comparison of oceanic and continental mantle lithosphere[J]. Physics of the Earth and Planetary Interiors, 309: 20.

Forsyth D W, Scheirer D S, Webb S C, et al. 1998. Imaging the deep seismic structure beneath a mid-ocean ridge: The MELT experiment[J]. Science, 280(5367): 1215-1218.

Fullea J. 2017. On joint modelling of electrical conductivity and other geophysical and petrological observables to infer the structure of the lithosphere and underlying upper mantle[J]. Surveys in Geophysics, 38(5): 963-1004.

Gao J, Zhang H J, Zhang S Q, et al. 2020. Magma recharging beneath the Weishan volcano of the intraplate Wudalianchi volcanic field, northeast China, implied from 3-D magnetotelluric imaging[J]. Geology, 48(9): 913-918.

Garcia X, Seillé H, Elsenbeck J, et al. 2015. Structure of the mantle beneath the Alboran Basin from magnetotelluric soundings[J]. Geochemistry, Geophysics, Geosystems, 16(12): 4261-4274.

Gardés E, Gaillard F, Tarits P. 2014. Toward a unified hydrous olivine electrical conductivity law[J]. Geochemistry Geophysics Geosystems, 15(12): 4984-5000.

Glover P W J, Hole M J, Pous J. 2000. A modified Archie's law for two conducting phases[J]. Earth and Planetary Science Letters, 180(3): 369-383.

Glover P W J. 2010. A generalized Archie's law for n-phases[J]. Geophysics, 75(6): E247-E265.

Guo H, Keppler H. 2019. Electrical conductivity of nacl-bearing aqueous fluids to 900 ℃ and 5 GPa[J]. Journal of Geophysical Research: Solid Earth, 124(2): 1397-1411.

Guo X, Yoshino T, Katayama I. 2011. Electrical conductivity anisotropy of deformed talc rocks and serpentinites at 3GPa[J]. Physics of the Earth and Planetary Interiors, 188(1): 69-81.

Guo X, Zhang L, Behrens H, et al. 2016. Probing the status of felsic magma reservoirs: Constraints from the P-T-H_2O dependences of electrical conductivity of rhyolitic melt[J]. Earth and Planetary Science Letters, 433: 54-62.

Guo X, Li B, Ni H, et al. 2017. Electrical conductivity of hydrous andesitic melts pertinent to subduction zones[J]. Journal of Geophysical Research: Solid Earth, 122(3): 1777-1788.

Guo X, Zhang L, Su X, et al. 2018. Melting inside the Tibetan crust? Constraint from electrical conductivity of Peraluminous granitic melt[J]. Geophysical Research Letters, 45(9): 3906-3913.

Guo Z, Wang K, Yang Y, et al. 2018. The origin and mantle dynamics of Quaternary intraplate volcanism in northeast China from joint inversion of surface wave and body wave[J]. Journal of Geophysical Research: Solid Earth, 123(3): 2410-2425.

Han J T, Kang J Q, Liu C, et al. 2019. Characteristics of the asthenosphere structure beneath the eastern segment of the Central Asia orogenic belt inferred from a long-period magnetotelluric survey[J]. Chinese Journal of Geophysics, 62(3): 1148-1158 (in Chinese).

Harmon N, Rychert C A, Kendall J M, et al. 2020. Evolution of the oceanic lithosphere in the equatorial Atlantic from Rayleigh wave tomography, evidence for small-scale convection from the PI-LAB experiment[J]. Geochemistry Geophysics Geosystems, 21(9): 18.

Hashim L, Gaillard F, Champallier R, et al. 2013. Experimental assessment of the relationships between electrical resistivity, crustal melting and strain localization beneath the Himalayan–Tibetan Belt[J]. Earth and Planetary Science Letters, 373: 20-30.

Heinson G, Didana Y, Soeffky P, et al. 2018. The crustal geophysical signature of a world-class magmatic mineral system[J]. Scientific Reports, 8(1): 10608.

Hermann J, Spandler C, Hack A, et al. 2006. Aqueous fluids and hydrous melts in high-pressure and ultra-high pressure rocks: Implications for element transfer in subduction zones[J]. Lithos, 92(3): 399-417.

Hier-Majumder S, Courtier A. 2011. Seismic signature of small melt fraction atop the transition zone[J]. Earth and Planetary Science Letters, 308(3): 334-342.

Hirschmann M M. 2010. Partial melt in the oceanic low velocity zone[J]. Physics of the Earth and Planetary Interiors, 179(1): 60-

71.

Hu X Y, Lin W L, Yang W C, et al. 2020. A review on developments in the electrical structure of craton lithosphere[J]. Science China Earth Sciences, 63(11): 1661-1677.

Huang X, Xu Y, Karato S-I. 2005. Water content in the transition zone from electrical conductivity of wadsleyite and ringwoodite[J]. Nature, 434(7034): 746-749.

Huang X G, Wang X, Chen Z A, et al. 2017. The experimental research on electrical conductivity for minerals and rocks under condition of upper mantle[J]. Scientia Sinica Terrae, 47(5): 518-529 (in Chinese).

Huang Y, Guo H, Nakatani T, et al. 2021. Electrical conductivity in texturally equilibrated fluid-bearing forsterite aggregates at 800℃ and 1 GPa: Implications for the high electrical conductivity anomalies in mantle wedges[J]. Journal of Geophysical Research: Solid Earth, 126(4): e2020JB021343.

Hübert J, Whaler K, Fisseha S. 2018. The electrical structure of the central main ethiopian rift as imaged by magnetotellurics: Implications for magma storage and pathways[J]. Journal of Geophysical Research: Solid Earth, 123(7): 6019-6032.

Iddon F, Edmonds M. 2020. Volatile-rich magmas distributed through the upper crust in the main ethiopian rift[J]. Geochemistry, Geophysics, Geosystems, 21(6): e2019GC008904.

Jenkins A P, Rust A C, Blundy J, et al. 2023. Magnetotelluric investigations at Andean volcanoes: Partial melt or saline magmatic fluids?[J]. Journal of Volcanology and Geothermal Research, 440: 17.

Ji W Q, Wu F Y. 2022. Volatile cycling and evolution of habitable environment on Earth[J]. Acta Petrologica Sinica, 38(5): 1285-1301 (in Chinese).

Johnson E R, Wallace P J, Cashman K V, et al. 2008. Magmatic volatile contents and degassing-induced crystallization at Volcán Jorullo, Mexico: Implications for melt evolution and the plumbing systems of monogenetic volcanoes[J]. Earth and Planetary Science Letters, 269(3): 478-487.

Johnson M C, Plank T. 2000. Dehydration and melting experiments constrain the fate of subducted sediments[J]. Geochemistry, Geophysics, Geosystems, 1(12): 1007.

Jones A G, Ferguson I J. 2001. The electric Moho[J]. Nature, 409(6818): 331-333.

Jones A G, Lezaeta P, Ferguson I J, et al. 2003. The electrical structure of the Slave craton[J]. Lithos, 71(2): 505-527.

Jones A G, Fishwick S, Evans R L, et al. 2013. Velocity-conductivity relations for cratonic lithosphere and their application: Example of Southern Africa[J]. Geochemistry, Geophysics, Geosystems, 14(4): 806-827.

Karato S-I. 2011. Water distribution across the mantle transition zone and its implications for global material circulation[J]. Earth and Planetary Science Letters, 301(3): 413-423.

Karato S-I. 2012. On the origin of the asthenosphere[J]. Earth and Planetary Science Letters, 321: 95-103.

Karato S-I, Wang D. 2013. Electrical Conductivity of Minerals and Rocks[M]// Karato S-I. Physics and Chemistry of the Deep Earth (First Edition). John Wiley & Sons Ltd, 145-182.

Karato S-I, Karki B, Park J. 2020. Deep mantle melting, global water circulation and its implications for the stability of the ocean mass[J]. Progress in Earth and Planetary Science, 7(1): 76.

Kasting J F, Catling D. 2003. Evolution of a habitable planet[J]. Annual Review of Astronomy and Astrophysics, 41: 429-463.

Kawakatsu H, Kumar P, Takei Y, et al. 2009. Seismic evidence for sharp lithosphere-asthenosphere boundaries of oceanic plates[J]. Science, 324(5926): 499-502.

Kawakatsu H, Utada H. 2017. Seismic and electrical signatures of the lithosphere–asthenosphere system of the normal oceanic mantle[J]. Annual Review of Earth and Planetary Sciences, 45: 139-167.

Kelbert A, Egbert G D, Schultz A. 2008. Non-linear conjugate gradient inversion for global EM induction: Resolution studies[J]. Geophysical Journal International, 173(2): 365-381.

Kelbert A, Schultz A, Egbert G. 2009. Global electromagnetic induction constraints on transition-zone water content variations[J]. Nature, 460(7258): 1003-1006.

Key K, Constable S, Liu L, et al. 2013. Electrical image of passive mantle upwelling beneath the northern East Pacific Rise[J]. Nature, 495(7442): 499-502.

Khan A, Shankland T J. 2012. A geophysical perspective on mantle water content and melting: Inverting electromagnetic sounding data using laboratory-based electrical conductivity profiles[J]. Earth and Planetary Science Letters, 317-318: 27-43.

Klumbach S, Keppler H. 2020. Electrical conductivity of HCl-bearing aqueous fluids to 700 ℃ and 1 GPa[J]. Contributions to Mineralogy and Petrology, 175(12): 10.

Kummerow J, Raab S, Schuessler J A, et al. 2020. Non-reactive and reactive experiments to determine the electrical conductivities of aqueous geothermal solutions up to supercritical conditions[J]. Journal of Volcanology and Geothermal Research, 391: 106388.

Kuvshinov A V. 2012. Deep electromagnetic studies from land, sea, and space: Progress status in the past 10 years[J]. Surveys in Geophysics, 33(1): 169-209.

Kuvshinov A, Semenov A. 2012. Global 3-D imaging of mantle electrical conductivity based on inversion of observatory C-responses—I. An approach and its verification[J]. Geophysical Journal International, 189(3): 1335-1352.

Laumonier M, Karakas O, Bachmann O, et al. 2019. Evidence for a persistent magma reservoir with large melt content beneath an apparently extinct volcano[J]. Earth and Planetary Science Letters, 521: 79-90.

Li S, Weng A, Zhang Y, et al. 2020. Evidence of bermuda hot and wet upwelling from novel three-dimensional global mantle electrical conductivity image[J]. Geochemistry, Geophysics, Geosystems, 21(6): e2020GC009016.

Li X, Ma X, Chen Y, et al. 2020. A plume-modified lithospheric barrier to the southeastward flow of partially molten Tibetan crust inferred from magnetotelluric data[J]. Earth and Planetary Science Letters, 548: 116493.

Li Y, Weng A, Xu W, et al. 2021. Translithospheric magma plumbing system of intraplate volcanoes as revealed by electrical resistivity imaging[J]. Geology, 49(11): 1337-1342.

Li Y, Weng A, Zhou Z, et al. 2024. Crustal root shapes the plumbing system of a monogenetic volcanic field as revealed by magnetotelluric data[J]. Earth and Planetary Science Letters, 626: 118523.

Liu J-Q, Erdmann S, Chen L-H, et al. 2021. Petrological evidence for magma recharge and mixing beneath the Ma'anshan monogenetic volcano of Xiaogulihe in Northeast China[J]. Lithos, 382-383: 105928.

Ma J, Deng Y, Li X, et al. 2025. Recent advances in machine learning-enhanced joint inversion of seismic and electromagnetic data[J]. Surveys in Geophysics, 46(1): 197-225.

Ma X P, Liu Y H, Yin C C, et al. 2024. Global mantle conductivity imaging using 3-D geomagnetic depth sounding with real earth surface conductivity constraint[J]. Computers & Geosciences, 192: 12.

Maier R, Heinson G, Thiel S, et al. 2007. A 3D lithospheric electrical resistivity model of the Gawler Craton, southern Australia[J]. Applied Earth Science, 116(1): 13-21.

Manning C E. 2004. The chemistry of subduction-zone fluids[J]. Earth and Planetary Science Letters, 223(1): 1-16.

Mckenzie D, Bickle M J. 1988. The volume and composition of melt generated by extension of the lithosphere[J]. Journal of Petrology, 29(3): 625-679.

Mehouachi F, Singh S C. 2018. Water-rich sublithospheric melt channel in the equatorial Atlantic Ocean[J]. Nature Geoscience, 11(1): 65-69.

Moorkamp M, Heincke B, Jegen M, et al. 2011. A framework for 3-D joint inversion of MT, gravity and seismic refraction data[J]. Geophysical Journal International, 184(1): 477-493.

Mu Q, Han J, Hou H, et al. 2022. Effect of the western Pacific plate subduction on upper mantle in the eastern segment of the Central Asian Orogenic Belt: Revealed by long-period magnetotelluric data[J]. Tectonophysics, 837: 229436.

Munch F D, Grayver A V, Guzavina M, et al. 2020. Joint inversion of daily and long-period geomagnetic transfer functions reveals lateral variations in mantle water content[J]. Geophysical Research Letters, 47(10): e2020GL087222.

Naif S, Key K, Constable S, et al. 2013. Melt-rich channel observed at the lithosphere-asthenosphere boundary[J]. Nature, 495(7441): 356-359.

Newman S, Lowenstern J B. 2002. VolatileCalc: A silicate melt–H_2O–CO_2 solution model written in visual basic for excel[J]. Computers & Geosciences, 28(5): 597-604.

Ni H W, Keppler H, Behrens H. 2011. Electrical conductivity of hydrous basaltic melts: Implications for partial melting in the upper mantle[J]. Contributions to Mineralogy and Petrology, 162(3): 637-650.

Olsen N. 1998. The electrical conductivity of the mantle beneath Europe derived from C-responses from 3 to 720 hr[J]. Geophysical Journal International, 133(2): 298-308.

Özaydin S, Selway K. 2020. MATE: An analysis tool for the interpretation of magnetotelluric models of the mantle[J]. Geochemistry Geophysics Geosystems, 21(9): 26.

Parker R L, Oldenburg D W. 1973. Thermal model of ocean ridges[J]. Nature-Physical Science, 242(122): 137-139.

Peacock J R, Mangan M T, Mcphee D, et al. 2015. Imaging the magmatic system of Mono Basin, California, with magnetotellurics in three dimensions[J]. Journal of Geophysical Research: Solid Earth, 120(11): 7273-7289.

Pearson D G, Brenker F E, Nestola F, et al. 2014. Hydrous mantle transition zone indicated by ringwoodite included within diamond[J]. Nature, 507(7491): 221-224.

Pommier A, Le-Trong E. 2011. "SIGMELTS": A web portal for electrical conductivity calculations in geosciences[J]. Computers & Geosciences, 37(9): 1450-1459.

Pommier A. 2014. Interpretation of magnetotelluric results using laboratory measurements[J]. Surveys in Geophysics, 35(1): 41-84.

Püthe C, Kuvshinov A, Khan A, et al. 2015. A new model of Earth's radial conductivity structure derived from over 10 yr of satellite and observatory magnetic data[J]. Geophysical Journal International, 203(3): 1864-1872.

Quist A S, Marshall W L. 1969. Electrical conductances of some alkali metal halides in aqueous solutions from 0 to 800. deg. and at pressures to 4000 bars[J]. The Journal of Physical Chemistry, 73(4): 978-985.

Rippe D, Unsworth M. 2010. Quantifying crustal flow in Tibet with magnetotelluric data[J]. Physics of the Earth and Planetary Interiors, 179(3): 107-121.

Rippe D, Unsworth M J, Currie C A. 2013. Magnetotelluric constraints on the fluid content in the upper mantle beneath the southern Canadian Cordillera: Implications for rheology[J]. Journal of Geophysical Research: Solid Earth, 118(10): 5601-5624.

Rooney T, Furman T, Bastow I, et al. 2007. Lithospheric modification during crustal extension in the Main Ethiopian Rift[J]. Journal of Geophysical Research: Solid Earth, 112(B10): B10201.

Rychert C A, Harmon N. 2018. Predictions and observations for the oceanic lithosphere from S-to-P receiver functions and SS precursors[J]. Geophysical Research Letters, 45(11): 5398-5406.

Rychert C A, Harmon N, Constable S, et al. 2020. The nature of the lithosphere-asthenosphere boundary[J]. Journal of Geophysical Research: Solid Earth, 125(10): 39.

Samrock F, Grayver A V, Bachmann O, et al. 2021. Integrated magnetotelluric and petrological analysis of felsic magma reservoirs: Insights from Ethiopian rift volcanoes[J]. Earth and Planetary Science Letters, 559: 10.

Saunders K, Blundy J, Dohmen R, et al. 2012. Linking petrology and seismology at an active volcano[J]. Science, 336(6084): 1023-1027.

Schilling J-G, Kingsley R H, Hanan B B, et al. 1992. Nd-Sr-Pb isotopic variations along the gulf of aden: Evidence for afar mantle plume-continental lithosphere interaction[J]. Journal of Geophysical Research: Solid Earth, 97(B7): 10927-10966.

Schmandt B, Jacobsen S D, Becker T W, et al. 2014. Dehydration melting at the top of the lower mantle[J]. Science, 344(6189): 1265-1268.

Schmidt M, Poli S. 2013. Devolatilization During Subduction[M]// Treatise on Geochemistry: vol 4: the Crust. Elsevier, 669-701.

Schmucker U. 1964. Anomalies of geomagnetic variations in the southwestern United States[J]. Journal of Geomagnetism and Geoelectricity, 15(4): 193-221.

Selway K. 2014. On the causes of electrical conductivity anomalies in tectonically stable lithosphere[J]. Surveys in Geophysics, 35(1): 219-257.

Selway K, Yi J, Karato S-I. 2014. Water content of the tanzanian lithosphere from magnetotelluric data: Implications for cratonic growth and stability[J]. Earth and Planetary Science Letters, 388: 175-186.

Selway K. 2019. Electrical Discontinuities in the Continental Lithosphere Imaged with Magnetotellurics [M]//Yuan H, Romanowicz B. Lithospheric Discontinuities. Washington, Amer Geophysical Union, 89-109.

Sheng Y, Jin S, Comeau M J, et al. 2021. Lithospheric structure near the northern Xainza-Dinggye Rift, Tibetan Plateau–Implications for rheology and tectonic dynamics[J]. Journal of Geophysical Research: Solid Earth, 126(8): e2020JB021442.

Sifré D, Gardés E, Massuyeau M, et al. 2014. Electrical conductivity during incipient melting in the oceanic low-velocity zone[J]. Nature, 509(7498): 81-85.

Sinmyo R, Keppler H. 2017. Electrical conductivity of NaCl-bearing aqueous fluids to 600 ℃ and 1 GPa[J]. Contributions to Mineralogy and Petrology, 172(1): 4.

Spratt J E, Skulski T, Craven J A, et al. 2014. Magnetotelluric investigations of the lithosphere beneath the central Rae craton, mainland Nunavut, Canada[J]. Journal of Geophysical Research: Solid Earth, 119(3): 2415-2439.

Stern R J. 2002. Subduction zones[J]. Reviews of Geophysics, 40(4): 3-1-3-38.

Sun J, Jin G, Bai D, et al. 2003. Sounding of electrical structure of the crust and upper mantle along the eastern border of Qinghai-Tibet Plateau and its tectonic significance[J]. Science in China Series D: Earth Sciences, 46(2): 243-253.

Sun J, Kelbert A, Egbert G D. 2015. Ionospheric current source modeling and global geomagnetic induction using ground geomagnetic observatory data[J]. Journal of Geophysical Research: Solid Earth, 120(10): 6771-6796.

Sun X Y, Zhan Y, Zhao L Q, et al. 2023. Does a shallow magma reservoir exist in the Wudalianchi volcanic field? Constraints from magnetotelluric imaging[J]. Geophysical Research Letters, 50(17): 10.

Syracuse E M, Van Keken P E, Abers G A. 2010. The global range of subduction zone thermal models[J]. Physics of the Earth and Planetary Interiors, 183(1): 73-90.

Tang Y, Obayashi M, Niu F, et al. 2014. Changbaishan volcanism in northeast China linked to subduction-induced mantle upwelling[J]. Nature Geoscience, 7(6): 470-475.

Ten Grotenhuis S M, Drury M R, Spiers C J, et al. 2005. Melt distribution in olivine rocks based on electrical conductivity measurements[J]. Journal of Geophysical Research: Solid Earth, 110(B12): B12201.

Thiel S, Heinson G. 2013. Electrical conductors in Archean mantle—Result of plume interaction?[J]. Geophysical Research Letters, 40(12): 2947-2952.

Tikhonov A. 1950. On determining electrical characteristics of the deep layers of the Earth's crust[J]. Proceedings of Academy of Sciences (USSR) Doklady, 83: 2295-2297.

Unsworth M, Wenbo W, Jones A G, et al. 2004. Crustal and upper mantle structure of northern Tibet imaged with magnetotelluric data[J]. Journal of Geophysical Research: Solid Earth, 109(B2): B02403.

Unsworth M J, Jones A G, Wei W, et al. 2005. Crustal rheology of the Himalaya and southern Tibet inferred from magnetotelluric data[J]. Nature, 438(7064): 78-81.

Unsworth M, Rondenay S. 2013. Mapping the Distribution of Fluids in the Crust and Lithospheric Mantle Utilizing Geophysical Methods[M]//Harlov D E, Austrheim H. Metasomatism and the Chemical Transformation of Rock: The Role of Fluids in Terrestrial and Extraterrestrial Processes. Berlin, Heidelberg; Springer Berlin Heidelberg, 535-598.

Valentine G A, Perry F V. 2007. Tectonically controlled, time-predictable basaltic volcanism from a lithospheric mantle source (central Basin and Range Province, USA)[J]. Earth and Planetary Science Letters, 261(1): 201-216.

Van Keken P E, Kiefer B, Peacock S M. 2002. High-resolution models of subduction zones: Implications for mineral dehydration reactions and the transport of water into the deep mantle[J]. Geochemistry, Geophysics, Geosystems, 3(10): 1056.

Wang D, Mookherjee M, Xu Y, et al. 2006. The effect of water on the electrical conductivity of olivine[J]. Nature, 443(7114): 977-980.

Wang D, Li H, Yi L, et al. 2010. Anisotropy of synthetic quartz electrical conductivity at high pressure and temperature[J]. Journal of Geophysical Research: Solid Earth, 115(B9): B09211.

Wang D, Guo Y, Yu Y, et al. 2012. Electrical conductivity of amphibole-bearing rocks: Influence of dehydration[J]. Contributions to Mineralogy and Petrology, 164(1): 17-25.

Wang S G, Constable S, Rychert C A, et al. 2020. A lithosphere-asthenosphere boundary and partial melt estimated using marine magnetotelluric data at the central middle atlantic ridge[J]. Geochemistry Geophysics Geosystems, 21(9): e2020GC009177.

Wang X, Zhang G, Fang H, et al. 2014. Crust and upper mantle resistivity structure at middle section of Longmenshan, eastern Tibetan Plateau[J]. Tectonophysics, 619-620: 143-148.

Wannamaker P E, Caldwell T G, Jiracek G R, et al. 2009. Fluid and deformation regime of an advancing subduction system at Marlborough, New Zealand[J]. Nature, 460(7256): 733-736.

Wei W, Unsworth M, Jones A, et al. 2001. Detection of widespread fluids in the Tibetan crust by magnetotelluric studies[J]. Science, 292(5517): 716-719.

Weitemeyer K A, Constable S, Tréhu A M. 2011. A marine electromagnetic survey to detect gas hydrate at Hydrate Ridge, Oregon[J]. Geophysical Journal International, 187(1): 45-62.

White R, Mckenzie D. 1989. Magmatism at rift zones: The generation of volcanic continental margins and flood basalts[J]. Journal of Geophysical Research: Solid Earth, 94(B6): 7685-7729.

Wilson C R, Spiegelman M, Van Keken P E, et al. 2014. Fluid flow in subduction zones: The role of solid rheology and compaction pressure[J]. Earth and Planetary Science Letters, 401: 261-274.

Worzewski T, Jegen M, Kopp H, et al. 2011. Magnetotelluric image of the fluid cycle in the Costa Rican subduction zone[J]. Nature Geoscience, 4(2): 108-111.

Xia Q-K, Liu J, Kovács I, et al. 2017. Water in the upper mantle and deep crust of eastern China: Concentration, distribution and implications[J]. National Science Review, 6(1): 125-144.

Xu G J, Tang J, Huang Q H, et al. 2015. Study on the conductivity structure of the upper mantle and transition zone beneath North China[J]. Chinese Journal of Geophysics, 58(2): 566-575 (in Chinese).

Xu Y G, Huang X L, Wang Q, et al. 2024. Earth's habitability driven by deep processes[J]. Chinese Science Bulletin, 69(2): 169-183 (in Chinese).

Xue S, Chen Y, Liang H, et al. 2021. Deep electrical resistivity structure across the Gyaring Co Fault in central Tibet revealed by magnetotelluric data and its implication[J]. Tectonophysics, 809: 228835.

Yang X, Keppler H, McCammon C, et al. 2011. Effect of water on the electrical conductivity of lower crustal clinopyroxene[J]. Journal of Geophysical Research: Solid Earth, 116(B4): B04208.

Yang X. 2012. Orientation-related electrical conductivity of hydrous olivine, clinopyroxene and plagioclase and implications for the structure of the lower continental crust and uppermost mantle[J]. Earth and Planetary Science Letters, 317-318: 241-250.

Yang X, McCammon C. 2012. Fe^{3+}-rich augite and high electrical conductivity in the deep lithosphere[J]. Geology, 40(2): 131-134.

Yang X, Keppler H, McCammon C, et al. 2012. Electrical conductivity of orthopyroxene and plagioclase in the lower crust[J]. Contributions to Mineralogy and Petrology, 163(1): 33-48.

Yang X Z. 2014. Electrical petrology: Principles, methods and advances[J]. Scientia Sinica Terrae, 44(9): 1884-1900 (in Chinese).

Yang Z, Li X, Deng Y, et al. 2025. Magnetotelluric evidence for lithospheric hydration and thinning beneath the Youjiang Basin in southwestern China[J]. Journal of Geophysical Research: Solid Earth, 130(2): e2024JB029650.

Yoshino T, Matsuzaki T, Yamashita S, et al. 2006. Hydrous olivine unable to account for conductivity anomaly at the top of the asthenosphere[J]. Nature, 443(7114): 973-976.

Yoshino T, Manthilake G, Matsuzaki T, et al. 2008a. Dry mantle transition zone inferred from the conductivity of wadsleyite and ringwoodite[J]. Nature, 451(7176): 326-329.

Yoshino T, Nishi M, Matsuzaki T, et al. 2008b. Electrical conductivity of majorite garnet and its implications for electrical structure in the mantle transition zone[J]. Physics of the Earth and Planetary Interiors, 170(3): 193-200.

Yoshino T, Katsura T. 2009. Effect of iron content on electrical conductivity of ringwoodite, with implications for electrical structure in the transition zone[J]. Physics of the Earth and Planetary Interiors, 174(1): 3-9.

Yoshino T, Matsuzaki T, Shatskiy A, et al. 2009. The effect of water on the electrical conductivity of olivine aggregates and its implications for the electrical structure of the upper mantle[J]. Earth and Planetary Science Letters, 288(1): 291-300.

Yoshino T, Katsura T. 2012. Re-evaluation of electrical conductivity of anhydrous and hydrous wadsleyite[J]. Earth and Planetary Science Letters, 337-338: 56-67.

Zhang B H, Xia Q K. 2021. Influence of water on the physical properties of olivine, wadsleyite, and ringwoodite[J]. European Journal of Mineralogy, 33(1): 39-75.

Zhang H, Egbert G D, Huang Q. 2022. A relatively dry mantle transition zone revealed by geomagnetic diurnal variations[J]. Science Advances, 8(31): eabo3293.

Zhang H, Egbert G D, Huang Q. 2023. Constraints on MTZ water content from joint inversion of diurnal variations and magnetospheric signals[J]. Geophysical Research Letters, 50(10): e2023GL102765.

Zhang Z, Deng Y, Xu Y-G, et al. 2024. A translithospheric magmatic system revealed beneath Changbaishan volcano[J]. Geology, 52 (10): 742-746.

Zhang Z M, Ding H X, Dong X, et al. 2020. Partial melting of subduction zones[J]. Acta Petrologica Sinica, 36(9): 2589-2615 (in Chinese).

Zhao D P, Toyokuni G, Kurata K. 2021. Deep mantle structure and origin of Cenozoic intraplate volcanoes in Indochina, Hainan and South China Sea[J]. Geophysical Journal International, 225(1): 572-588.

Zhao G, Unsworth M J, Zhan Y, et al. 2012. Crustal structure and rheology of the Longmenshan and Wenchuan M_W 7.9 earthquake epicentral area from magnetotelluric data[J]. Geology, 40(12): 1139-1142.

Zhao L Q, Zhan Y, Hu Y X, et al. 2024. The deep magma system in the Longgang intraplate monogenetic volcano of Jilin Province revealed by 3D magnetotelluric method[J]. Chinese Journal of Geophysics, 67(11): 4220-4232 (in Chinese).

Zhao W B, Guo Z F, Lei M, et al. 2019. Volcanogenic CO_2 degassing in the Songliao continental rift system, NE China[J]. Geofluids, 2019: 14.

Zhao Y-H, Ginsberg S B, Kohlstedt D L. 2004. Solubility of hydrogen in olivine: Dependence on temperature and iron content[J]. Contributions to Mineralogy and Petrology, 147(2): 155-161.

Zheng Y F, Xia Q X, Chen R X, et al. 2011. Partial melting, fluid supercriticality and element mobility in ultrahigh-pressure metamorphic rocks during continental collision[J]. Earth-Science Reviews, 107(3): 342-374.

Zheng Y F, Chen Y X, Dai L Q, et al. 2015. Developing plate tectonics theory from oceanic subduction zones to collisional orogens[J]. Science China Earth Sciences, 58(7): 1045-1069.

Zheng Y F, Chen Y X. 2016. Continental versus oceanic subduction zones[J]. National Science Review, 3(4): 495-519.

Zhu S, Deng Y, Zhang Z, et al. 2024. Geophysical-petrological modelling of the crust and upper mantle structure across the north-south gravity lineament in NE China: Insights into the lithospheric thinning mechanism[J]. Terra Nova, 36(2): 148-160.

附中文参考文献

陈克非，林叶，申文豪，等. 2023. 腾冲火山起源的地球物理和地球化学研究进展[J]. 地球与行星物理论评(中英文)，54(2)：216-230.

韩江涛，康建强，刘财，等. 2019. 中亚造山带东段软流圈分布特征——基于长周期大地电磁探测的结果[J]. 地球物理学报，62(3)：1148-1158.

胡祥云，林武乐，杨文采，等. 2020. 克拉通岩石圈电性结构研究进展[J]. 中国科学：地球科学，50(11)：1533-1552.

黄晓葛，王欣欣，陈祖安，等. 2017. 上地幔矿物和岩石电导率的实验研究[J]. 中国科学：地球科学，47(5)：518-529.

纪伟强，吴福元. 2022. 地球的挥发分循环与宜居环境演变[J]. 岩石学报，38(5)：1285-1301.

徐光晶，汤吉，黄清华，等. 2015. 华北地区上地幔及过渡带电性结构研究[J]. 地球物理学报，58(2)：566-575.

徐义刚，黄小龙，王强，等. 2024. 地球宜居性的深部驱动机制[J]. 科学通报，69(2)：169-183.

杨晓志. 2014. 电导岩石学：原理、方法和进展[J]. 中国科学：地球科学，44(9)：1884-1900.

张泽明，丁慧霞，董昕，等. 2020. 俯冲带部分熔融[J]. 岩石学报，36(9)：2589-2615.

赵凌强，詹艳，胡亚轩，等. 2024. 三维大地电磁方法揭示的吉林龙岗板内单成因火山深部岩浆系统[J]. 地球物理学报，67(11)：4220-4232.

郑永飞，陈伊翔，戴立群，等. 2015. 发展板块构造理论：从洋壳俯冲带到碰撞造山带[J]. 中国科学：地球科学，45(6)：711-735.